Lithos 324–325 (2019) 402–417

Contents lists available at ScienceDirect

Lithos

journal homepage: www.elsevier.com/locate/lithos

# Cretaceous (~100 Ma) high-silica granites in the Gajin area, Central Tibet: Petrogenesis and implications for collision between the Lhasa and Qiangtang Terranes

Zong-Yong Yang [a,b], Qiang Wang [a,b,c,*], Chunfu Zhang [d], Jin-Hui Yang [e], Lin Ma [a], Jun Wang [a,b], Peng Sun [a,b], Yue Qi [a,b]

[a] State Key Laboratory of Isotope Geochemistry, Guangzhou Institute of Geochemistry, Chinese Academy of Sciences, Guangzhou 510640, China
[b] College of Earth and Planetary Sciences, University of Chinese Academy of Sciences, Beijing 100049, China
[c] CAS Center for Excellence in Tibetan Plateau Earth Sciences, Beijing 100101, China
[d] Department of Geosciences, Fort Hays State University, Hays, KS 67601-4099, USA
[e] Institute of Geology and Geophysics, Chinese Academy of Science, Beijing 100029, China

ARTICLE INFO

*Article history:*
Received 11 August 2018
Accepted 12 November 2018
Available online 15 November 2018

*Keywords:*
High-silica granites
Magmatic lull
Continental collision
Cretaceous
Tibet

ABSTRACT

High-silica granites that occur as isolated plutons are widely distributed in collisional orogenic belts and are considered a hallmark of continental collision processes. The late Mesozoic collision between the Lhasa and Qiangtang Terranes along the Bangong–Nujiang Suture Zone was key event in the evolution of the Tibetan Plateau; however, the timing of this collision remains debated. Here, we report the ages and geochemical characteristics of granites from the Gajin area in the north-central Lhasa Terrane, central Tibet. Zircon U—Pb dating reveals that the Gajin granites formed at ~100 Ma. These granites exhibit uniformly high $SiO_2$ contents (74.9–78.4 wt%), are weakly peraluminous compositions, and have high $K_2O$, moderate $Na_2O$ and $Al_2O_3$, and low $Fe_2O_3^T$, MgO, and CaO contents. They are characterized by enrichments in Rb, Cs, and U, and by depletions in Zr, Hf, Nb, and Ti. These characteristics, in combination with high Rb/Sr ratios and pronounced negative Eu anomalies, indicate that the Gajin granites are highly fractionated rocks. The granites have enriched whole-rock Nd ($\varepsilon_{Nd}[t] = -4.3$ to $-2.9$) and relatively depleted and slightly variable zircon Hf ($\varepsilon_{Hf}[t] = -1.0$ to $+5.5$) isotope compositions. The Gajin granites were probably generated by high degrees of crystal fractionations of magma produced by partial melting of mature crustal sources. The Cretaceous magmatic rocks in the north-central Lhasa Terrane record a magmatic lull between ~100 and 85 Ma, which corresponds to a transition in both geochemical composition (e.g., Hf—Nd isotopes) and rock association at ~100 Ma. Combining the above characteristics with the development of a regional angular unconformity around the time of the formation of the granites, we suggest that the initial continental collision between the Lhasa and Qiangtang Terranes probably occurred between 110 and 90 Ma. Therefore, the ~100 Ma high-silica granites in the Gajin area were formed during the continuing continental convergence that followed the initial collision between the Lhasa and Qiangtang Terranes. The generation of discrete and monotonous high silica granites may constitute evidence for a significant tectonothermal transition in evolution of the continental crust.



## 1. Introduction

Intrusive rocks containing >70 wt% silica are termed silica-rich or high-silica granites (Lee and Morton, 2015). These granites are widely distributed in many orogenic belts and include the Proterozoic Harney Peak granites of the Trans-Hudson orogenic belt (Nabelek and Liu, 2004), the leucogranites of the Teton Range of Wyoming (Frost et al., 2016), the Mesoproterozoic leucogranites of the Kaoko belt, Namibia (Jung et al., 2012), the Late Cretaceous Xiuwacu granites in the Yidun Terrane, eastern Tibet (Wang et al., 2014b), and the leucogranites of the Cenozoic Himalayan orogenic belt (e.g., Le Fort, 1981; Liu et al., 2016; Ma et al., 2017b; Zhang et al., 2004). Generally, these granitic rocks are distinct and uniform in their geochemical compositions, and are genetically important in most orogenic belts (Jung et al., 2012; Le Fort, 1981). In addition, as an element of the Neoarchean continental crust, these high-silica granites also occur in old cratons (Bagdonas et al., 2016; Laurent et al., 2014; Moyen et al., 2003).

There is a long-standing controversy as to whether chemical signatures in high-silica igneous rocks are derived by fractional

* Corresponding author at: State Key Laboratory of Isotope Geochemistry (SKLaBIG), Guangzhou Institute of Geochemistry (GIG), Chinese Academy of Sciences (CAS), Wushan Street, Guangzhou 510640, China.
*E-mail address:* wqiang@gig.ac.cn (Q. Wang).

https://doi.org/10.1016/j.lithos.2018.11.011
0024-4937/

crystallization (Lee and Morton, 2015; Tindle and Pearce, 1981; Wu et al., 2017) or partial melting (Frost et al., 2016; Nabelek and Liu, 2004). In a continental arc, thickened crust and lithosphere are considered favorable for the generation of high-silica granites (Lee et al., 2007). Moreover, such granites are generally associated with coeval gabbros, diorites, tonalites, and granodiorites (Lee et al., 2007); however, in a collision zone these granites are ascribed either to the crystal fractionation of more mafic magmas or the partial melting of meta-sedimentary or meta-igneous rocks (Frost et al., 2016; Jung et al., 2012; Wu et al., 2017). Compared with those found in continental arc settings, high-silica granites in collision belts are rarely associated with coeval mafic-intermediate rocks (e.g., gabbros, diorites, and granodiorites) (Le Fort, 1981; Wu et al., 2017; Zhang et al., 2004). These collision-belt granites commonly occur as discrete plutons and are synchronous with or post-date a collisional event (Sylvester, 1998; Zhang et al., 2004). The formation of such granites may be related to processes occurring during continental collision and subsequent crustal thickening (Le Fort, 1981; Zhang et al., 2004). Consequently, these granites are commonly considered a hallmark of continental collision processes (Frost et al., 2016; Ma et al., 2017b; Nabelek and Liu, 2004); however, the triggering mechanisms for the origin of granites with uniformly high silica content ("restricted-range high-silica granites") in collision orogenic belt and that formed at the end of Archean remain unresolved (e.g., Laurent et al., 2014).

The Qiangtang and Lhasa terranes are important elements of the Tibetan Plateau and collided with each other during the late Mesozoic; however, there is no consensus regarding the timing of amalgamation/collision between these two terranes. The chronological constraints for this event range from the Middle Jurassic through the latest Jurassic to the Early Cretaceous, based on geological and paleomagnetic data (Hao et al., 2016, 2018; Ma et al., 2017a; Zhu et al., 2016, and references therein). The recently identified bathyal to abyssal turbidites of the late Early Cretaceous Zhaga Formation and the Zhonggang ocean island basaltic rocks from the Gerze area (Fan et al., 2018, and references therein) indicate that the Bangong–Nujiang Ocean closed at the end of the Early Cretaceous.

Abundant late Mesozoic volcanic rocks and granitoids are found in the northern Lhasa and southern Qiangtang terranes (Chen et al., 2017a; Hao et al., 2016; Li et al., 2015; Zhu et al., 2016). Based on the occurrence of these magmatic rocks, the collision between the Lhasa and Qiangtang terranes is thought to have occurred during the the Early Cretaceous (~140 Ma) (Zhu et al., 2016) or late Early Cretaceous (~110 Ma) (Fan et al., 2018; Hao et al., 2016, 2018; Li et al., 2015; Li et al., 2017a).

The late Mesozoic igneous rocks in the northern Lhasa and southern Qiangtang terranes recorded the period from early Bangong-Nujiang oceanic slab subduction to subsequent continental collision between the Qiangtang and Lhasa terranes. In this study, we report the chronology and geochemistry of the high-silica granites in the Gajin area, north-central Lhasa Terrane, central Tibet. These Cretaceous (~100 Ma) granites occur as isolated plutons and are comparable to the Cenozoic Himalayan high-silica granites in terms of their geochemistry and geology. The granites in the Gajin area provide important new information regarding the timing of the collision between the Lhasa and Qiangtang terranes.

## 2. Geological setting

The Tibetan Plateau consists of four continental terranes (from north to south) including the Songpan-Ganzi, Qiangtang, Lhasa, and Himalanyan (Pan et al., 2012). The Bangong-Nujiang Suture Zone (BNSZ) of central Tibet (Fig. 1a), which extends east-west for over 1500 km (Wang et al., 2016; Zhang et al., 2017), separates the Qiangtang Terrane to the north from the Lhasa Terrane to the south. The Lhasa Terrane can be further divided into northern, central, and southern subterranes, separated by the Shiquan River-Nam Co Mélange Zone (SNMZ) and the Luobadui-Milashan Fault (LMF), respectively (e.g., Zhu et al., 2016). Dismembered mafic and ultramafic rocks are distributed along the BNSZ, the basalts among them having an affinity to mid-ocean ridge basalt (MORB) or ocean island basalt (OIB) and being considered as residual Tethyan oceanic crust (Wang et al., 2016 and references therein; Zhang et al., 2017). Geochronological data suggest that the ages of those mafic rocks range from ~250 to ~110 Ma (Wang et al., 2016). The OIB-type pillow basalt interbedded with bioclastic limestone and red chert in the Tarenben and Duoma areas was erupted at ~108 Ma (Wang et al., 2016; Zhu et al., 2016).

Extensive Jurassic and Cretaceous magmatic rocks occur on both sides of the BNSZ (Hao et al., 2016, 2018; Li et al., 2017a; Zhu et al., 2016) and have been explained in terms of the subduction of the Banong-Nujiang Ocean and continental collision (Chen et al., 2017a; Hao et al., 2016; Li et al., 2015; Zhu et al., 2016). Cretaceous volcanic rocks in the north-central Lhasa Terrane include the Zenong Group and the Duoni Formation, with the Qushenla Formation being located to the south of the BNSZ (Zhu et al., 2016, and references therein). The Early Cretaceous Zenong Group (eruption age ~114 Ma, Chen et al., 2014b) contains mainly high-K calc-alkaline series felsic lavas and volcaniclastic rocks, has a mean thickness of over 1000 m, and covers an area of ~20,000 $km^2$ (Zhu et al., 2016, and references therein). The Duoni Formation consists mainly of andesites with subordinate dacitic and rhyolitic lavas, has a thickness of exceeding 3000 m locally, and yields Early Cretaceous eruption ages of ~115–100 Ma (Zhu et al., 2016, and references therein). The sparsely distributed Qushenla Formation consists of andesites and minor basaltic andesites and pyroclastic rocks (Zhu et al., 2016). The Early Cretaceous granitoids are widespread (~16,000 $km^2$) in the north-central Lhasa Terrane (Fig. 1a), and consist of granodiorites and monzogranites with mafic microgranular enclaves (Zhu et al., 2016). Late Cretaceous magmatic rocks are sporadic and limited in volume (Chen et al., 2015; Sun et al., 2015; Wang et al., 2014a).

The basements of the central and northern parts of the Lhasa Terrane consist of Precambrian metamorphic rocks and juvenile crust materials, respectively (Xu et al., 1985; Zhu et al., 2016). In the Gajin area (Fig. 1b) of the north-central Lhasa Terrane, Precambrian quartz-schist of the Nyainqentanglha Group is unconformably overlain by the Paleozoic strata. The Carboniferous–Permian strata are composed mainly of siliciclastic rocks that overlie a lower Paleozoic limestone-dominated sequence (Zhang et al., 2012). The Gajin granites intrude the Carboniferous–Permian sandstones and argillaceous slates and volcanic-sedimentary rock of the Early Cretaceous Zenong Group. The contact metamorphic zones between the plutons and the wall rocks indicate the allochthonous emplacement of the plutons. An angular unconformity separates the Lower Cretaceous marine strata from the Upper Cretaceous–Tertiary succession (Kapp et al., 2007; Zhang et al., 2012), indicating crustal uplift. The Jingzhushan Formation molasses deposits along the BNSZ recorded the collapse of the orogenic belt that related to the continental collision between the Lhasa and Qiangtang terranes (Li et al., 2015; Pan et al., 2012).

## 3. Petrographic characteristics

The Gajin plutons are exposed in central part of the Lhasa Terrane and consist of two discrete intrusions exposed over a total area of ~260 $km^2$ (Fig. 1b). These granites are intruded into the upper Paleozoic sedimentary rocks and volcanic rocks of the Early Cretaceous Zenong Group (Chen et al., 2014b). Small outcrops of Precambrian mylonite, two-mica schist, and quartz schist of the Nyainqentanglha Group (Hu et al., 2005) occur west of the eastern pluton. These metamorphic rocks are in fault contact with the Paleozoic sedimentary rocks. The western intrusion has been cut by several normal faults. There is no other obvious deformation and metamorphism, and both intrusions are devoid of crustal metamorphic xenoliths or magma-derived mafic microgranular enclaves.

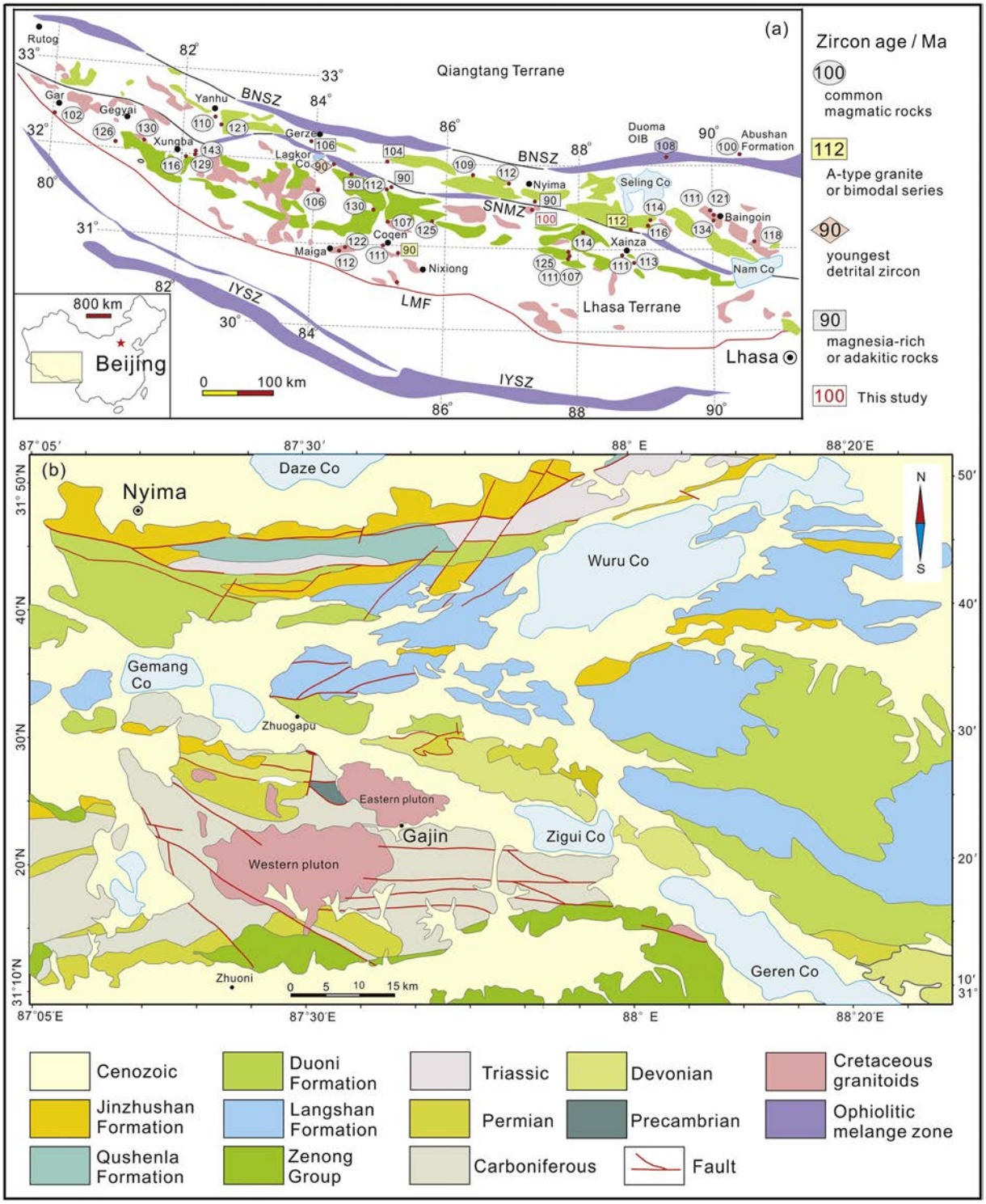


**Fig. 1.** Sketch-maps showing (a) the distribution and emplacement ages of major igneous rocks in the Lhasa Terrane, southern Tibet (after Zhu et al., 2016, and references therein); and (b) geology of the Gajin area. BNSZ-Bangongco-Nujiang Suture Zone; IYSZ-Indus-Yarlung Suture Zone; SNMZ-Shiquan River-Nam Co Mélange Zone; LMF-Luobadui-Milashan Fault.

The Gajin plutons consist of pink to gray granites with medium- to fine-grained granular or local porphyritic textures (Fig. 2). Rocks with porphyritic texture contain ~30 vol% phenocrysts of 0.5–2.0 cm in size (Fig. 2c). These phenocrysts include subhedral to euhedral plagioclase (10 vol%), anhedral quartz (5 vol%), subhedral alkali-feldspar (5 vol%), and biotite (<5 vol%). The groundmass comprises mainly quartz (25 vol%), alkali-feldspar (20 vol%), plagioclase (20 vol%), and biotite (<3 vol%) as well as minor Fe—Ti oxides. The medium- to fine-grained rocks have homogeneous and hypidiomorphic granular textures (Fig. 2d) at the outcrop scale and contain alkali-feldspar (35 vol%), quartz (30 vol%), plagioclase (20–30 vol%), biotite (<5 vol%), and Fe—Ti oxides (ilmenite and Ti-magnetite) (<3 vol%). Small aplite dykes measuring a few centimeters in width cuts the plutons. The contact between different rock phases is gradational (Fig. 2a), which indicates they are coeval magma products. The accessory minerals of all these rocks are similar and include apatite, zircon, allanite. Sericitization and argillization of feldspars and chloritization of biotites are observed in some samples.

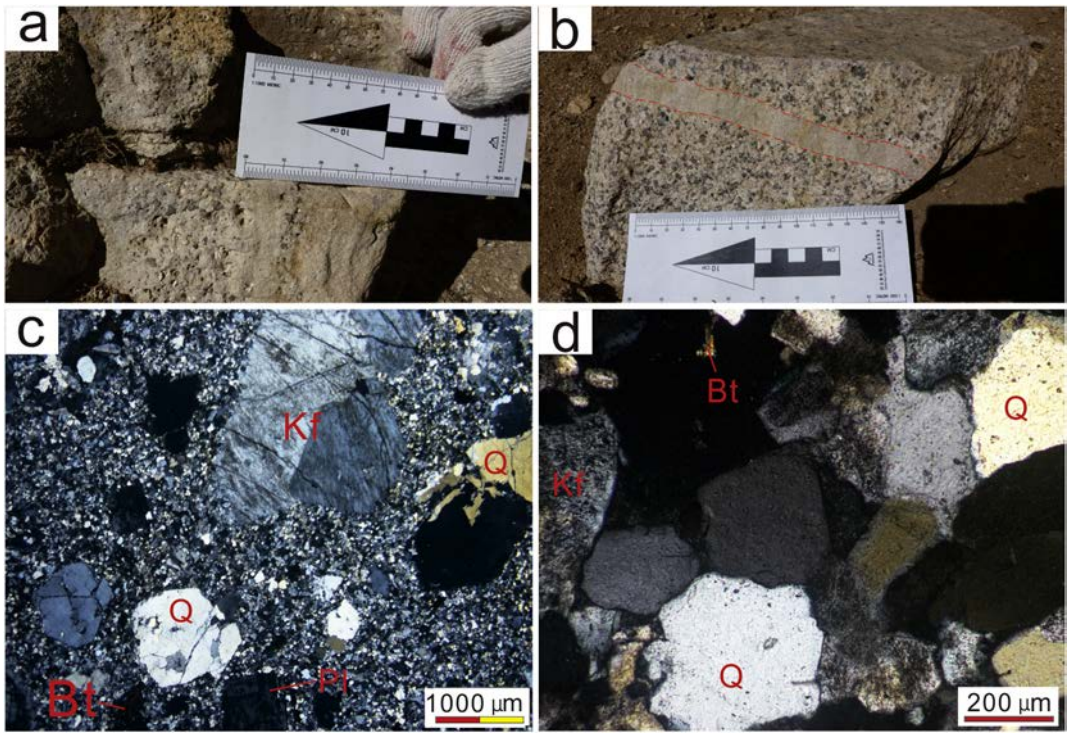


**Fig. 2.** (a) and (b) Field photographs showing the contact relationships between the various rocks; (c) and (d) Photomicrographs showing the porphyritic and fine-grained granular textures of the Ganjin granites, respectively. Abbreviations: Q = quartz, Kf = K-feldspar, Pl = plagioclase, Bt = biotite.

## 4. Analytical methods

### *4.1. Zircons U—Pb dating and Hf isotope analyses*

Laser-ablation-multi-collector–inductively coupled plasma–mass spectrometry (LA–MC–ICP–MS) zircon U—Pb dating and Hf isotopic analyses were conducted on three zircon samples (16NM18–1 and 16NM19–2 from the western pluton, 16NM21–4 from the eastern pluton). Zircon U—P isotopic ratios and trace element concentrations are list in Supplementary Table S1, the zircon Hf isotope data are show in Supplementary Table S2.

Each sample (>3 kg) was cleaned with water, crushed to small fragments, and then subjected to standard density and magnetic separation techniques to concentrate zircons. Zircon grains were hand-picked under a stereographic microscope and then the selected zircon grains were mounted in an epoxy resin cylinder and polished to expose the interiors of crystals for analysis. Cathodoluminescence (CL) images were taken of all zircon grains to assess their internal structures using a JEOL JXA-8100 Superprobe at the State Key Laboratory of Isotope Geochemistry, Guangzhou Institute of Geochemistry, Chinese Academy of Sciences (SKLaBIG, GIG–CAS), Guangzhou, China.

Zircon U—Pb dating was conducted at the Institute of Geology and Geophysics, Chinese Academy of Sciences (IGG-CAS) in Beijing, and at the Guilin University of Technology, Guilin, China. An Agilent 7500a ICP-MS instrument combined with a 193 nm excimer ArF LA system was used to simultaneously determine zircon U—Pb isotopic ratios and trace element concentrations. The detailed operating conditions for the LA system and ICP-MS instrument, as well as off-line data calculations, were similar to those described by Liu et al. (2008). The Isoplot/EX v.3.0 program (Ludwig, 2003) was used for calculating the weighted mean U—Pb ages and for the Tera-Wasserburg concordia plots. Uncertainties for individual analyses are reported at the 1-sigma level; mean ages for pooled $^{206}Pb/^{238}U$ results are quoted at the 2-sigma level. The zircon standard Temora yielded an weighted mean age of 416.9 ± 2.1 Ma (n = 16), which agrees well with the recommended value (Black et al., 2003). The $^{206}Pb/^{238}U$ age of 594 ± 11 Ma (n = 6) for the unknown zircon GJ-1 is in agreement with the recommended ID–TIMS age within error (Wiedenbeck et al., 1995).

In situ Lu—Hf isotope analyses were conducted after U—Pb dating using LA–MC–ICP–MS instrument at Guilin University of Technology. A beam diameter of 60 μm and a laser pulse frequency of 8 Hz were used. For details of the analytical procedure and equipment operating conditions see Wu et al. (2006). During the analysis period, the standard GJ-1 (analyzed as an unknown) yielded a weighted mean $^{176}Hf/^{177}Hf$ ratio of 0.282019 ± 0.000018 (n = 31), in agreement with the recommended value (Morel et al., 2008).

### *4.2. Whole-rock major and trace elements*

Fresh or least altered samples (~1 kg) were crushed and powdered with a carbide mortar. Twelve samples from the western pluton and nine samples from the eastern pluton were selected for major and trace element analyses. Each individual sample was mixed with $Li_2B_4O_7$ and melted in a platinum crucible. Fused glass beads were used for determining of major-element oxides with a Rigaku RIX 2000 X-ray fluorescence spectrometer at the SKLaBIG, GIG–CAS. The calibration lines used for quantification were obtained by bivariate regression of data from 36 reference materials. The analytical uncertainties are in the range of 1% to 5%. Concentrations of trace elements were determined using an ICP-MS Perkin-Elmer Sciex ELAN 6000 instrument at the SKLaBIG, GIG–CAS. The analytical procedures used were similar to those of Li et al. (2006). The analytical precisions are commonly better than 5%. The analytical results are reported in Supplementary Table S3.

### *4.3. Whole-rock Nd isotopic compositions*

Whole-rock Nd isotope analyses (5 samples from the western pluton and 4 samples from the eastern pluton) were performed using a Micromass Isoprobe MC–ICP–MS instrument at the SKLaBIG, GIG–CAS. The chemical separation and purification of Nd was achieved using cation-exchange resin with HDEHP-coated Kef columns. Details of the procedures and analytical conditions used are described by Li et al. (2006).

Measured $^{143}Nd/^{144}Nd$ ratios were fractionation corrected to $^{146}Nd/^{144}Nd = 0.7219$. The Shin Etsu JNdi-1 standard gave a mean $^{143}Nd/^{144}Nd$ ratio of 0.512103 ± 0.000005 (n = 9) during the analytical procedure. The Nd isotope data are listed in Supplementary Table S4.

## 5. Results

### 5.1. Zircon U—Pb geochronology

The LA–ICP–MS zircon U—Pb isotope data for the Gajin granites are displayed in Fig. 3. Most of the analyzed zircon grains are of magmatic origins, as inferred from the zircon oscillatory zoning observed in CL images (Fig. 3) and from the high Th/U ratios (0.4–7.2). For zircon U—Pb dating, two granite samples were selected from the western intrusion and one from the eastern intrusion. For the western intrusion, 19 of the 24 spots analyzed for sample 16NM18–1 (coordinate: N31° 15′ 52.1″, E87° 10′ 34.2″) yield a weighted mean age of 101 ± 1 Ma (MSWD = 1.1) and 19 of 21 spots analyzed for the fine-grained granite (16NM19–2, coordinate: N31° 22′ 53.1″, E87° 34′ 39.9″) from western intrusion yield a weighted mean age of 100 ± 1 Ma (MSWD = 0.6). Thus, the crystallization age of the western intrusion should be ~100 Ma. For the eastern intrusion, 15 of 21 zircon grains analyzed for sample 16NM21–4 (coordinate: N31° 23′ 4″, E87° 39′ 39.7″) yield a weighted mean age of 100 ± 1 Ma (MSWD = 0.2). This age is indistinguishable

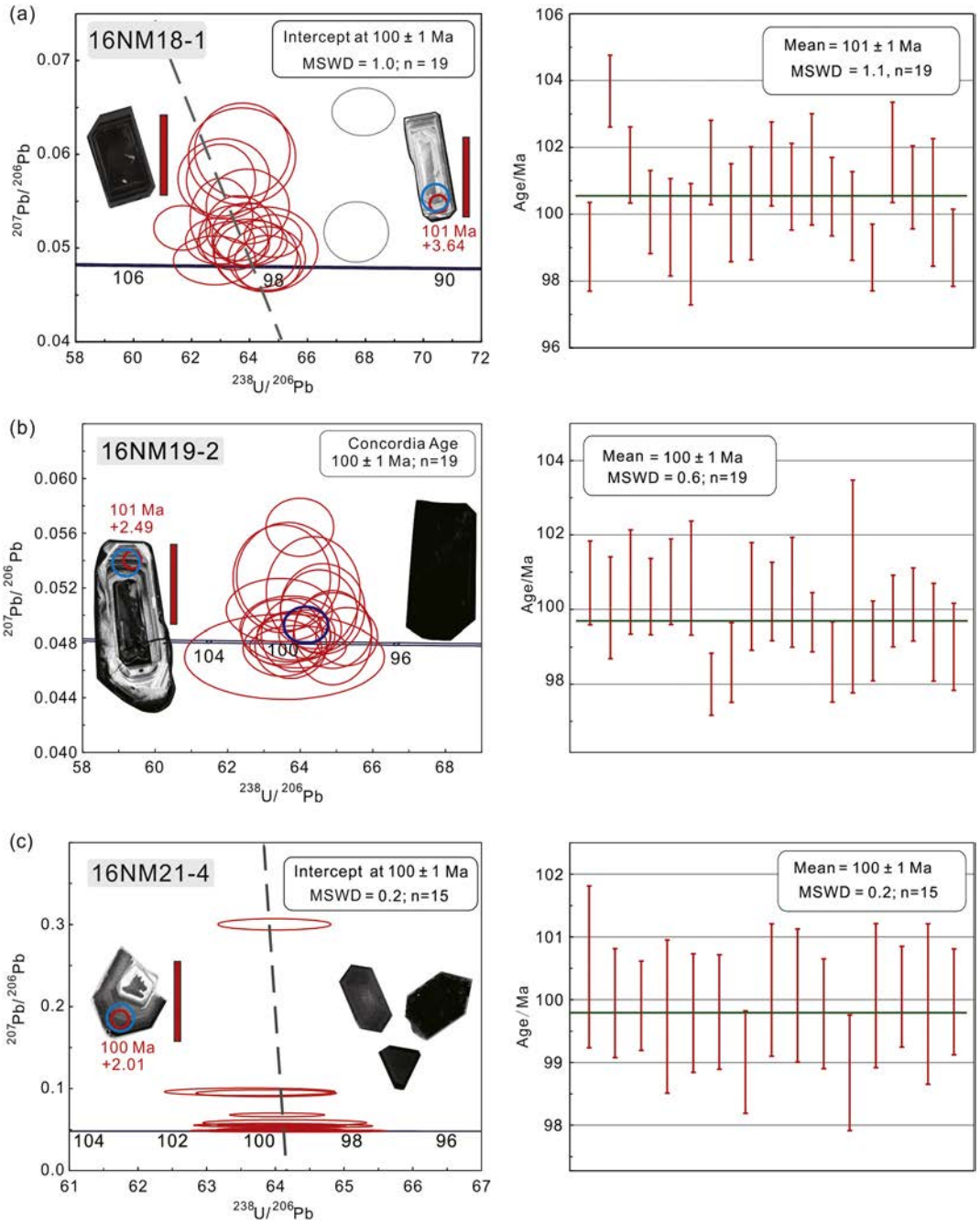


**Fig. 3.** Cathodoluminescence (CL) images of representative zircons and Tera-Wasserburg plots for the Gajin granite samples 16NM18–1 (a) and 16NM19–4 (b) of the western pluton, and 16NM21–4 (c) of the eastern pluton. The scale bars adjacent to the zircon CL images are 100 μm. The solid red and blue circles in the zircon CL images indicate the locations of U—Pb and Hf isotopic analyses, respectively. The numbers near the analysis spots are the apparent $^{206}U/^{238}Pb$ ages and $\varepsilon_{Hf}(t)$ values, respectively. (For interpretation of the references to colour in this figure legend, the reader is referred to the web version of this article.)

from that of the western pluton. In summary, the zircon U—Pb dating results indicate that the Gajin granites were generated at the Early–Late Cretaceous boundary (~100 Ma).

### 5.2. Whole-rock geochemistry

The Gajin granites are characterized by uniformly high silica contents (74.9–78.4 wt%), similar to high-silica granites elsewhere (e.g., Frost et al., 2016). The Gajin samples have somewhat low $Al_2O_3$ (12.0–13.5 wt %) and moderate to high total alkali contents (ranging from 7.5–9.0 wt %) that are comparable to those of Himalayan leucogranites (Liu et al., 2016; Zhang et al., 2004). Consequently, the Gajin granites range from syenogranite to alkali-feldspar granite (Fig. 4a). They are peraluminous with alumina saturation index A/CNK (defined by $Al_2O_3/(CaO + Na_2O + K_2O)$ in molar proportions) values >1.0 (Fig. 4b). In addition, the granites have low CaO (<1.0 wt%), $P_2O_5$ (≤0.04 wt%), and low abundances of ferromagnesian oxides: $Fe_2O_3^T$ (0.8–2.2 wt%), MgO (<0.4 wt%), MnO (<0.1%), and $TiO_2$ (<0.2 wt%) (Fig. 5).

Primitive mantle-normalized multi-element plots of the Gajin granites (Fig. 6b) show pronounced enrichments in strongly incompatible elements (e.g., Rb, Th, and U) and depletions in high field strength elements (HFSE: e.g., Nb, Ta, and Ti). The Gajin granites have high total rare earth element (REE) contents (64.9–316.8 ppm, with the exception of sample 16NM19–2 with 32.5 ppm) and show moderate fractionation of heavy REE (HREE) relative to light REE (LREE) (Fig. 6a. chondrite-normalized La/Yb ratios vary from 1.5 to 10.4, and samples 16NM21–1 and 16NM19–2 exhibit LREE depletion relative to HREE). Most samples show marked depletions in Eu (Fig. 6a), with Eu/Eu* values of 0.004–0.572, ($Eu/Eu^* = Eu_N/(Sm_N \times Gd_N)^{1/2}$, where subscript N indicates chondrite-normalized).

### 5.3. Whole-rock Nd and zircon Hf isotopic compositions

Initial isotopic ratios of the Gajin granites were calculated at 100 Ma. These granites have slightly variable initial $^{143}Nd/^{144}Nd$ ratios of 0.512291–0.512364, with $\varepsilon_{Nd}(t = 100\ Ma)$ values of −4.25 to −2.87 (Fig. 7a). The granites have high and variable zircon $\varepsilon_{Hf}$ (t) values (Fig. 8) and positive $\Delta\varepsilon_{Hf}(t)$ values (3.31–10.03) (Fig. 7b) (where $\Delta\varepsilon_{Hf}[t] = \varepsilon_{Hf}[t] - 1.55 \times \varepsilon_{Nd}[t] + 1.21$) and plot close to or above the terrestrial array (Vervoort et al., 2011).

## 6. Discussion

### 6.1. Petrogenesis

#### 6.1.1. Fractional crystallization

Crustal assimilation was limited in the generation of the Gajin granites. The studied granites have the highest silica contents of all the magmatic rocks reported from the Lhasa Terrane (e.g., Zhu et al., 2016, and references therein), and there is no negative relationship between whole-rock $\varepsilon_{Nd}(t)$ values and the $SiO_2$ contents. Also, no wall-rock rafts or crustal xenoliths have been found to date. The narrow range of zircon $\varepsilon_{Hf}(t)$ values (Fig. 8b–d) and the relatively homogeneous whole-rock Nd isotopic values (Fig. 7a), in conjunction with the absence of mafic microgranular enclaves suggest that mixing of mantle-derived mafic and crust-originated melt did not take place in the formation of the Gajin granites.

The geochemical features of the Gajin granites indicate that crystal fractionation was critical during magmatic evolution. The systematic trends in major-element oxide covariation plots (Fig. 5) indicate the occurrence of fractional crystallization. The negative correlations of $Al_2O_3$ and CaO contents with $SiO_2$ content indicate the precipitation and separation of plagioclase (Fig. 5b, d). This is consistent with the significant negative Eu and Sr anomalies of the Gajin granites (Figs. 6 and 9), as plagioclases has large partitioning coefficients for Eu and Sr. Apatite fractionation may explain the negative slopes between the CaO and $SiO_2$ (Fig. 5d) and between $P_2O_5$ and $SiO_2$ contents (Fig. 5f), as well as the pronounced depletions in $P_2O_5$. Decreasing $Fe_2O_3^T$, MgO, and $TiO_2$ concentrations with increasing $SiO_2$ may have resulted from the crystallization of biotite, which is the only mafic mineral found in the plutons. The western and eastern plutons show slightly different distributions on a ($Na_2O + K_2O$) vs. $SiO_2$ diagram, and the slight negative slope between the $Na_2O$ and $SiO_2$ and the positive correlation between $K_2O$ and $SiO_2$ for the western pluton indicate that plagioclase, and K-feldspar are the dominant crystallization phase (Fig. 9). This interpretation is supported by the occurrence of subhedral to euhedral alkali-feldspar phenocrysts, the significant negative Eu anomalies (Fig. 6a) and the pronounced depletions of Sr and Ba (Fig. 6b) in the primitive mantle-normalized spidergrams.

The low MgO contents and resultantly in high FeO*/MgO ratios (6.1 to 101.6) of the Gajin granites are similar to those of A-type granites (e.g., Huang et al., 2008). While, the calculated whole-rock Zr saturation temperature (746–831 °C), and the low concentrations of HFSEs (e.g., Zr + Nb + Ce + Y = 153–383 ppm), and the absence of alkalic mafic minerals in combination with the low 10,000*Ga/Al ratios (2.6–3.8), all indicate that the Gajin granites are highly fractionated granites, rather than A-type granites (Eby, 1990). The high Rb/Sr ratios (2.7–248.3) and rather low Zr/Hf and Nb/Ta ratios (15–34 and 4.3–12.7, respectively) are additional evidence for the highly evolved nature of the Gajin granites (e.g., Chen et al., 2014a; Guo et al., 2012; Liu et al., 2016). In addition, the low K/Rb ratios (from 60 to 153) and the convex REE tetrad effects of some samples indicate a high degree of crystal fractionation (Liu et al., 2016; Wu et al., 2017).

The low viscosity required for extensive fractional crystallization in the Gajin magmas could have been brought about by relatively high temperature and involvement of vapor or liquid. The estimated

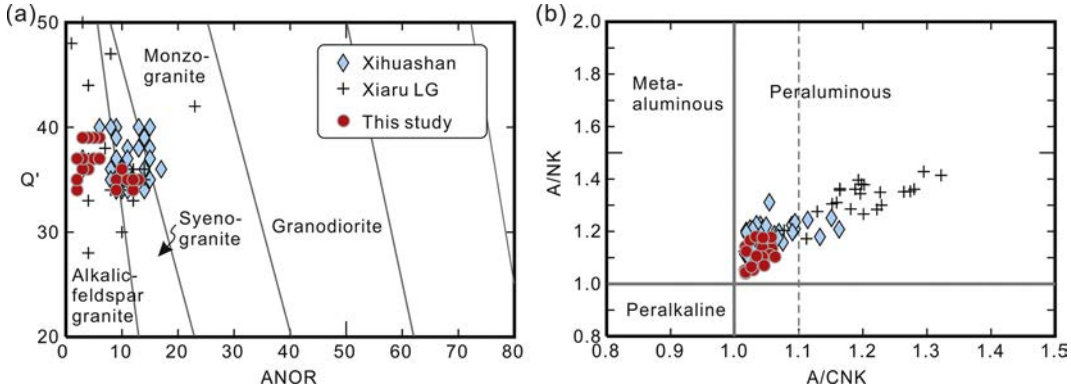


**Fig. 4.** (a) Q'-ANOR normative composition diagram (Streckeisen and Le Maitre, 1979) and (b) A/NK–A/CNK diagram for classifying of the Gajin granites. $Q' = Q/(Q + Or + Ab + An) \times 100$; $ANOR = An/(Or + An) \times 100$. $A = Al_2O_3$, $N = Na_2O$, $K = K_2O$, $C = CaO$ (all in molar proportion). Data for the Xihuashan granites in South China are from Guo et al. (2012), and for the Xiaru leucogranites (LG) in the Himalayan are from Liu et al. (2016).

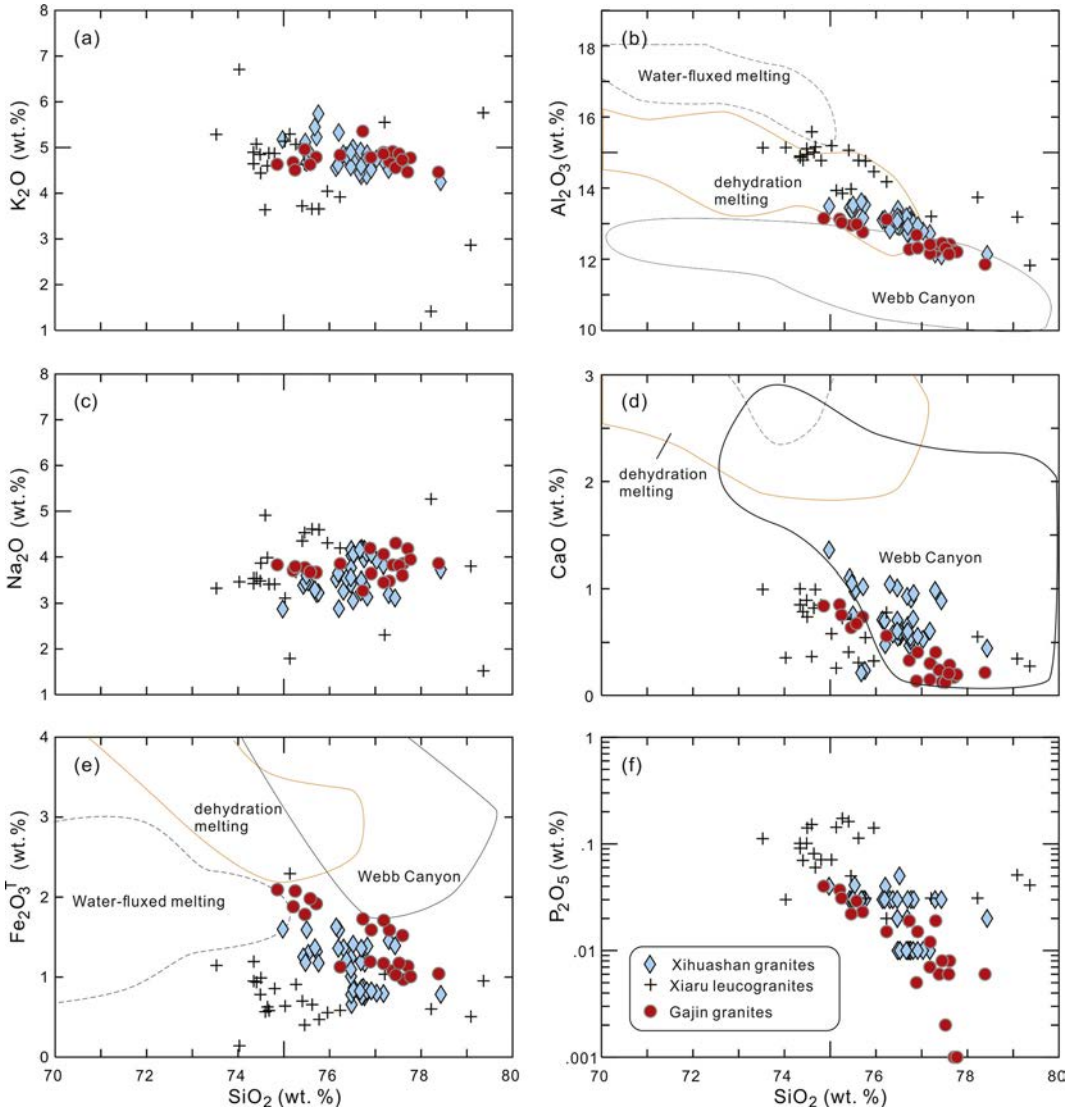


**Fig. 5.** Selected chemical variation diagrams for the Gajin granites. The field for the Webb Canyon leucogranite is from Frost et al. (2016). The fields defined for experimental melt formed by dehydration and for the water-fluxed melting of mafic rocks at moderate to low pressures are modified from Beard and Lofgren (1991). Data for the Xihuashan granites in South China are from Guo et al. (2012) and for the Xiaru leucogranites in the Himalayan are from Liu et al. (2016).

temperature (~700–880 °C), based on whole-rock Zr saturation (Watson and Harrison, 1983) and Ti-in-zircon (Ferry and Watson, 2007) methods, is variable and high, which would have reduced magma viscosity. In addition, geochemical modeling (see Section 6.1.2) and petrographic features of the Gajin granites indicate feldspar was the dominant phase during magma differentiation. The crystallization of large amount of anhydrous minerals would have increased the fraction of liquid of the residual melts. Liquids that are enriched in

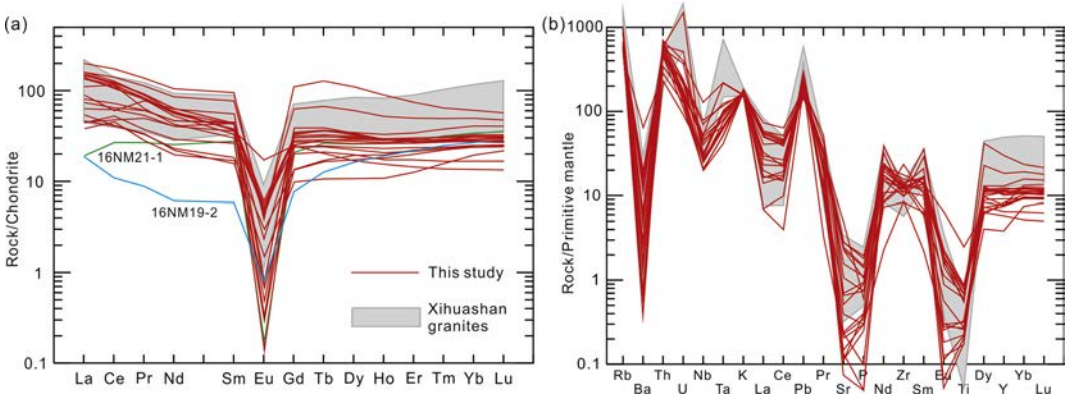


**Fig. 6.** (a) Chondrite-normalized REE patterns and (b) primitive mantle-normalized trace elements spidergrams for the Gajin granites. The normalization values are from Sun and McDonough (1989). Data for the Xihuashan granites in South China are from Guo et al. (2012).

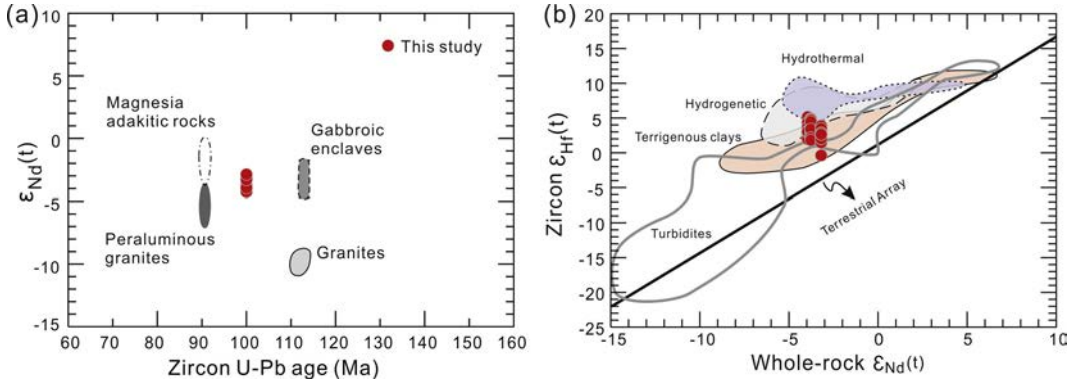


**Fig. 7.** Whole-rock Nd isotope composition vs. zircon U—Pb age diagram (a) and zircon $\varepsilon_{Hf}(t)$ vs. whole-rock $\varepsilon_{Nd}(t)$ diagram (b) for the Gajin granites. The terrestrial array in (b) is given by the following equation: whole-rock $\varepsilon_{Hf}(t) = 1.55 \times \varepsilon_{Nd}(t) + 1.21$ (after Vervoort et al., 2011). Data for the ~90 Ma adakatic rocks and peraluminous granites are from Chen et al. (2015), and for the Early Cretaceous gabbroic enclaves and granites are from Zhu et al. (2016) and references therein.

water and fluorine can substantially reduce the viscosity of $SiO_2$-rich magmas (Baker and Vaillancourt, 1995; Giordano et al., 2004). Fluid enrichment is indicated by the REE tetrad effect with low K/Rb ratios (60–153) (Wu et al., 2017, and references therein) observed for the analyzed granites, as well as by the presence of some zircon grains similar with those formed under volatile-saturated conditions or in the presence of F-rich fluid (Zeng et al., 2017).

### 6.1.2. Geochemical modeling

Major-elements mass balance calculations and strongly incompatible trace element modeling were used to assess the likelihood of fractional crystallization. As the studied granite samples are evolved, determining the possible compositions of the parental magmas is made more difficult than otherwise. Given this constraint, the modeling of trace element evolution provides general trends rather than precise details because the error bars on coefficients are quite large (e.g., Tindle and Pearce, 1981).

*6.1.2.1. Major element mass balance calculations.*. The results of the major-element mass balance calculations are given in Table 1, and compositions of fractionated mineral, parental magma and derivative liquid are reported in Supplementary Table S5a. Choosing the upper continental crust (UCC) as the parental magma allows exploration of whether the Gajin granites were generated by common magmas derived from continental crust. In model 1, the residual liquid (Gajin granites, 16NM19–1) can be reproduced by ~ 40% crystal fractionation of plagioclase, clinopyroxene, orthopyroxene, biotite, and ilmenite from a less-felsic magma (UCC). The low sum of the squares of residuals ($\sum R^2 = 0.9871$) indicate the modeling is reasonable.

Model 2 was run to test the feasibility of the most highly evolved liquid (16NM18–2) being generated by fractional crystallization from less

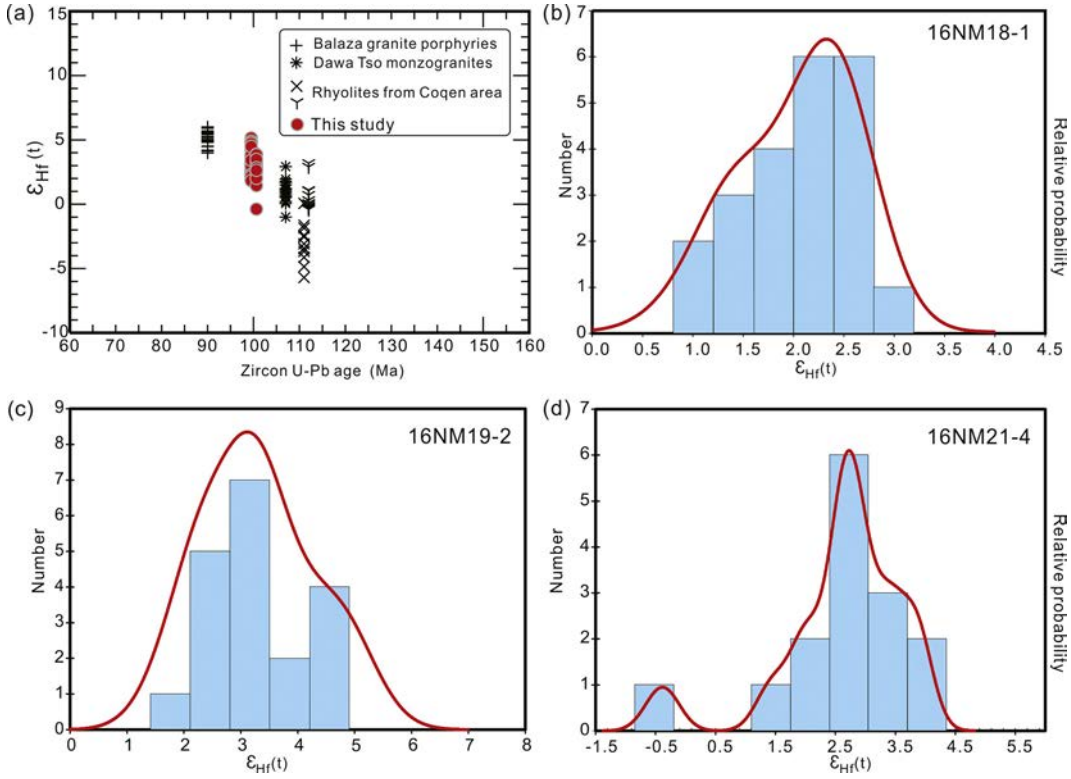


**Fig. 8.** (a) Zircon $\varepsilon_{Hf}(t)$ values vs. zircon age diagram and (b)–(d) histograms and relative probabilities of $\varepsilon_{Hf}(t)$ values of the Gajin granites. The Balaza granite porphyry (Li et al., 2017a), the Dawa Tso maonzogranites and rhyolites (Zhu et al., 2016, and references therein) from the Coqen area of the Lhasa Terrane are plotted for comparison.

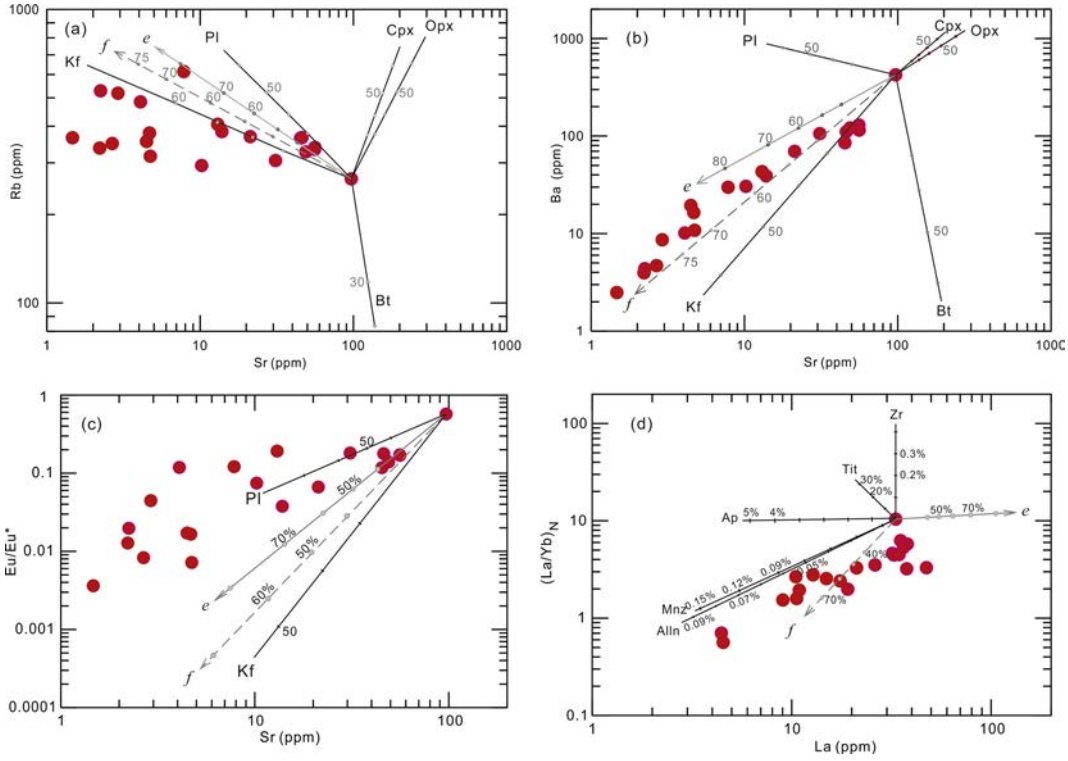


**Fig. 9.** (a) Rb, (b) Ba, and (c) Eu/Eu* vs. Sr plots, and (d) $(La/Yb)_N$ vs. La plot for the Gajin granites. Mineral abbreviations: Alln – allanite, Ap – apatite, Bt – biotite, Cpx – clinopyroxene, Kf – K-feldspar, Mnz – monazite, Opx – orthopyroxene, Pl – plagioclase, Tit – titanite, Zr – zircon.

evolved magma (16NM19–1). Beyond ~11 wt% fractional crystallization of clinopyroxene, plagioclase, K-feldspar, biotite, and ilmenite, the residual liquid composition corresponds well with the composition of sample 16NM18–2, with a low value of $\sum R^2$ (0.0033).

The highly evolved liquid (16NM18–2) can be modeled by ~46 wt% crystal fractionation of a magma that is similar to UCC in composition, with a modal mineral assemblage of orthopyroxene + clinopyroxene + plagioclase + K-feldspar + biotite + ilmenite being removed. The $\sum R^2$ of 1.0441 implies this model is acceptable.

*6.1.2.2. Trace element modeling.* To further investigation the evolution of the Gajin granites, we used Rb, Sr, Ba for trace element modeling. These elements are affected mainly by the major minerals during magma differentiation. After then, depletion in Eu was modeled. Sample 16NM18–4, which shows moderate Eu depletion (Eu/Eu* = 0.57) and relatively high Sr, and Ba contents, was used as an initial magma in trace elements modeling. Partitioning coefficients, the fractionated mineral assemblages, and modeling results are listed in Supplementary Table S5b-c.

When a fractionated mineral assemblage (assemblage "e" in Fig. 10: 25 wt% Kf + 55 wt% Pl + 10 wt% Cpx + 10 wt% Bt) that broadly similar to modeling result of mass balance calculation model 2 is applied, the marked Eu negative anomalies of the Gajin granites can be roughly reproduced by ~60% fractional crystallization (Fig. 10). The modeled residual liquids have Rb, Sr, Ba contents (Fig. 9) that are similar to the mean values of these elements in the more evolved eastern pluton (Supplementary Table S5c). The strongest Eu depletion can be modeled with a ~75% degree of fractionation of the same mineral association. Closer correspondences of the modeled liquid concentrations of those elements and the mean values could be obtained by change the fractionated mineral modal (such as mineral assemblage "f").

However, the extreme enrichment in Rb (613 ppm), and the depletions in Sr (3 ppm), and Ba (10 ppm) could not be perfectly modeled when the measured Eu depletion was reproduced (Figs. 9-10), even after applying a large degree of fractionation (>60%) of a mineral modal composition containing a high proportion of K-feldspar (up to 45%) or changing the partition coefficients (Supplementary Table S5c) (e.g., Mackenzie et al., 1988). The extreme depletion in Eu resemble that observed for beryl- and topaz-bearing amazonite granite from Xinjiang, northwestern China, which were produced by fractional crystallization accompanied by fluid-melt interaction (Gu et al., 2011; Tindle and Pearce, 1981).

*6.1.2.3. Nb—Ta fractionation.* Variation in Nb/Ta may indicate the crystal-melt fractionation of a Ti-rich mineral for a restricted range of melt compositions. More importantly, at a wider scale it may indicate fluid-related fractionation (Ballouard et al., 2016; Green, 1995).

The partition coefficients for Nb and Ta of Ti-rich minerals are from Stepanov et al. (2014), and those for other minerals are from www.

**Table 1**
Results of mass balance calculations with least square method.

| Model No. | Parental compostion | Minerals removed out recalculated to 100% | | | | | | Fractionation degree % | Residual liquid | $\sum R^2$ |
|---|---|---|---|---|---|---|---|---|---|---|
| | | Opx | Cpx | Pl | Kf | Bt | Ilm | | | |
| 1 | UCC | 13.59 | 16.68 | 61.63 | – | 5.31 | 2.79 | 40.36 | 16NM19–1 | 0.9871 |
| 2 | 16NM19–1 | – | 9.88 | 51.67 | 20.81 | 9.48 | 8.17 | 10.62 | 16NM18–2 | 0.0033 |
| 3 | UCC | 10.46 | 16.66 | 60.52 | 0.78 | 8.31 | 3.26 | 45.69 | 16NM18–2 | 1.0441 |

Opx = orthopyroxene, Cpx = clinopyroxene, Pl = plagioclase, Kf = K-feldspar, Bt = Biotite, Ilm = ilmenite.

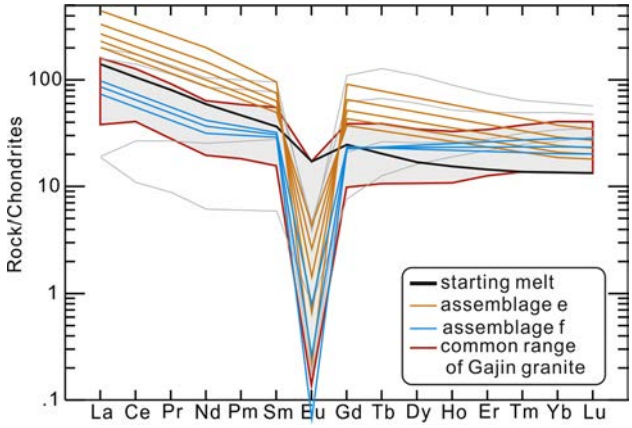


**Fig. 10.** REE modeling results. The total REE concentrations and depletion of Eu increase with differentiation of the modeled mineral assemblage "e". LREEs decrease drastically with the addition of a small amount of monazite in the fractionated mineral assemblage "f". In both these two mineral assemblages, the pronounced Eu negative anomalies can be reproduced by a high degree of fractional crystallization.

earthref.org/GERM and tabulated in Supplementary Table S5d. When a mineral assemblage similar to the model result of the mass balance calculation model 2 is adopted, the modeled Nb/Ta ratios are higher than those of the Gajin granites (Fig. 11a). The modeling of a fictional mineral association with a high proportion of biotite (10% Cpx + 40% Pl + 30% Kf + 20% Bt) can reproduce the observed Ta and Nb/Ta ratios if ~75% fractionation is assumed; however, such a high degree of fractional fractionation is unreasonable. A dramatic reduction in whole-rock $SiO_2$ content would be anticipated when sequentially removing this mineral assemblage, the narrow range of $SiO_2$ variation (~2 wt%) from the sample with the highest Nb/Ta to the lowest is inconsistent with this scenario.

*6.1.2.4. Zr—Hf fractionation.* Previous studies have attributed lower-than-chondrite Zr/Hf ratios to zircon fractionation (Gelman et al., 2014; Linnen and Keppler, 2002). The Hf concentrations of the Gajin granites decrease slightly with differentiation, with the eastern pluton showing a wider spread of values than the eastern pluton. In contrast, the Gajin granites show whole-rock Zr concentration decreased consistently with the progressive evolution, with the corresponding Zr/Hf ratios decreasing from a near-chondrite value (~34) to sub-chondrite value (~14) with magma fractionation.

Zircon accommodates most of the Zr of calc-alkali peraluminous granitic rocks because Zr is a major structural constituent of zircon; however, the partitioning of Zr in zircon and melt does not follow Henry's Law and is difficult to estimate. Therefore, a pseudo-coefficient value of 2 was used for Zr in the total fractionated minerals and residual melts (Gelman et al., 2014). The assumptions made in modeling the Zr—Hf fractionation were that the Hf is affected mainly by zircon and the total amount of zircon accounts for ~0.05 wt% of the whole-rock. Sample 16NM18–4 was used as the starting magma. The lowest Zr/Hf ratio of the Gajin granites was able to be modeled with ~70% zircon fractionation (Fig. 11b).

*6.1.2.5. Role of fluid.* The trace element modeling of Rb, Sr, Ba, and Eu presented above shows that the depletions in Ba, Sr, and Eu, as well as the enrichment in Rb, could not be well modeled simultaneously (Fig. 9). This may partly reflect the wide variation in coefficients used in the modeling, but may also be related to fluid-related processes in the magma (Tindle and Pearce, 1981). The scatter of negative Eu anomalies with decreasing Sr concentration and the consistently low in Ba and Sr contents of the eastern pluton relative to the western pluton could indicate that fluid influenced the late-stage evolution of the magma that produced the Gajin granites. The wider range in Hf concentration with increasing Rb/Sr ratio of the eastern pluton, relative to the western pluton, might also have been caused by fluids. Such an interpretation is supported by zircon grains in the eastern pluton (Fig. 3c) that show features consistent with metamict zircon remobilization by alteration and dissolution during magmatic-hydrothermal transition (e.g., Zeng et al., 2017). Furthermore, some of the studied samples show REE tetrad effects, which have been interpreted as resulting from the interaction between fluids and residual melt (e.g., Wu et al., 2017; Yang et al., 2018).

*6.1.3. Crustal melting*

As contemporaneous mafic magmas are rare throughout the north-central Lhasa Terrane, the primitive magmas of the Gajin granites are likely to have been produced by the melting of mature continental materials. Mineral modal compositions (high modal proportions of quartz and K-feldspar, and low in mafic minerals) and major (Fig. 5) and trace elements (Rb, Sr, and Ba) suggest that the Gajin granites have geochemical compositions similar to those of leucogranites (e.g., Frost et al., 2016; Le Fort, 1981; Liu et al., 2016; Ma et al., 2017b). The formation of peraluminous granites has been explained by fluid-fluxed melting (Le Fort, 1981) or vapor-absent melting of fertile crustal quartzofeldspathic rocks (Patiño Douce and Beard, 1995). The lowest Rb/Sr ratio (2.7) among the analyzed samples is higher than that of upper continental crust (2; e.g., Rudnick and Gao, 2003), also providing support for the above conclusion. The eastern pluton shows greater chemical differentiation than does the western pluton, but the former is slightly less evolved in whole-rock Nd isotope (−3.76 to −4.25 of western intrusion and − 2.87 to −3.30 of eastern intrusion), although there are no appreciable distinctions in their zircon Hf isotopes. This observation can be explained by the disequilibrium partial melting of metapelite through various degrees of parent-daughter fractionation (Zeng et al., 2005), or by the involvement of juvenile crustal components (Chen et al., 2014a).

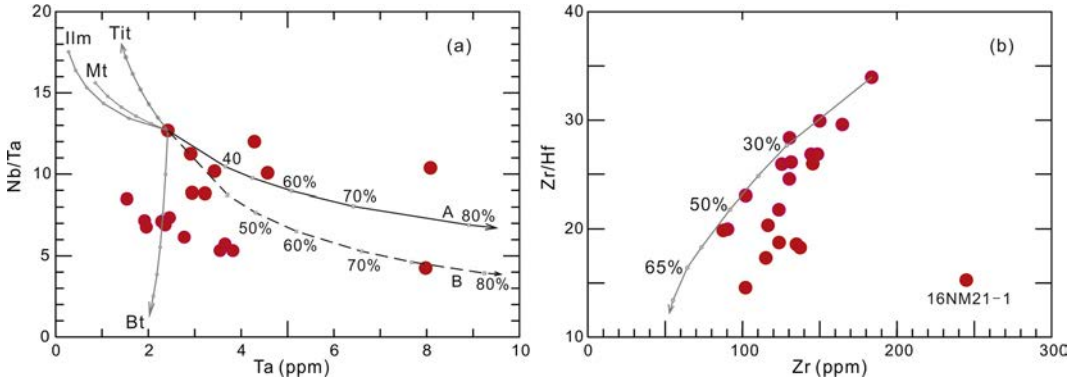


**Fig. 11.** (a) Nb—Ta and (b) Zr—Hf modeling results. The range of Nb/Ta ratios of the Gajin granites can be approximately modeled with mineral assemblage that includes a high proportion of biotite. The observed low Zr/Hf ratios of the Gajin pluton are reproduced with a high fraction of zircon fractionation. In (a), vector A contains a lower proportion of biotite (10%) than vector B (20%). Values adjacent to the curved vectors are the degree of fractionation in %. Mineral abbreviation: Mt. – magnetite; others same as in Fig. 9.

The late Mesoproterozoic–early Neoproterozic two-stage modal ages obtained from whole-rock Nd and zircon Hf analyses indicate that the ancient crustal component was the dominant source, and the ~780 Ma Nyainqentanglha Group metamorphic rocks (Hu et al., 2005) from central Lhasa Terrane are a suitable candidate source for this melting event. We conclude this on the basis of the following observations. 1) The whole-rock Nd and zircon Hf isotope compositions of the Gajin granites indicate Mesoproterozoic-Neoproterozoic two-stage depleted-mantle model ages. Cenozoic granitic gneiss and migmatite from the central Lhasa Terrane contain Mesoproterozoic inherited or captured zircons, and these rocks yield Mesoproterozoic Nd model ages (Hu et al., 2005; Xu et al., 1985). 2) The Nyainqentanglha Group metamorphic rocks consist of Proterozoic meta-sedimentary and meta-volcanic rocks. Meta-mafic rocks from this rock suite yield $\varepsilon_{Nd}(t = 100\ Ma) = -4$ to $+4$ (Hu et al., 2005), broadly similar to that of the Cretaceous Gajin granites in the north-central Lhasa Terrane. 3) The Nyainqentanglha Group metamorphic rocks, which are a potential source of the Gajin granites, crop out adjacent to the studied plutons (Fig. 1b). 4) Late Cretaceous andesites of the Zhuogapu area, which are considered to represent the melting of delaminated mafic lower crust, crop out ~20 km north of the Gajin granites and have whole-rock Nd and zircon Hf (Wang et al., 2014a) characteristics similar to those of the Gajin granites.

There is a marked decoupling of the zircon Hf isotopes ($\varepsilon_{Hf}[t] = 0.5$ to 5.5) and the whole-rock Nd isotopes ($\varepsilon_{Nd}[t] = -2.9$ to $-4.3$) of the Gajin granites (Fig. 7b). The involvements of garnets or sediments in the partial melting are alternative interpretations of this observation (e.g., Jiang et al., 2012). As garnets have higher coefficients for HREEs than for LREEs, the derivative magmas should have low HREE contents and high $(La/Yb)_N$ ratios if garnets are remnants after partial melting; however, the relatively low $(La/Yb)_N$ ratios (0.6 to 10.4, with a mean of 3.5) and high Yb contents (>2.3 ppm, averaging 5 ppm) of the Gajin granites indicate that there was no significant garnet effect.

Therefore, the Hf − Nd isotope decoupling of the Gajin granites could be easily reconciled by the involvement of sediments in the source region (Marini et al., 2005). The low $CaO/Na_2O$ ratios (<0.3) of the Gajin granites (Fig. 12) are similar to those of typical peraluminous granites generated by the melting of pelites (e.g., Le Fort, 1981; Liu et al., 2016; Zhang et al., 2004). In addition, the Th contents of the Gajin granites (18.3–55.3 ppm) are comparable to those of Cenozoic Himalaya leucogranites (e.g., Liu et al., 2016; Zhang et al., 2004) and tourmaline-bearing two-mica rhyolites of northern Tibet (Wang et al., 2012). The high Th/La ratios of the Gajin granites (0.67–12.18) also suggest melting of the source region involving sediments.

Source characteristics can be inferred from geochemical data because the melt compositions depend heavily on the source compositions and the conditions of partial melting (Clemens and Vielzeuf, 1987; Wang et al., 2012). Magmas produced within the garnet stability field should have low concentrations of HREE and Y similar to adakitic rocks (e.g., Ou et al., 2017). The behavior of Y is similar to that of HREE, and it is strongly partitioned to garnet and hornblende. The high Y and HREE concentrations of the Gajin granites may indicate the melting of source rocks outside the stability field of garnet or hornblende during the generation of magmas, and the partial melting would have occurred at a relatively shallow crust level, possibly no deeper than the middle continental crust at pressure of <8 Kbar (e.g., Wang et al., 2012). Low CaO and $Al_2O_3$ contents are additional indicators of the occurrence of partial melting within the pressure range for plagioclase stability. Although the low CaO and $Al_2O_3$ contents could also result from plagioclase fractional crystallization, those features are at least indicative of the melting within the plagioclase stability field. Quartz and feldspar dominated the composition of the Gaijin granite, accounting for the narrow range of high $SiO_2$ contents. This restriction in the range of $SiO_2$ is similar to that of the Webb Canyon leucogranites from Wyoming area (Frost et al., 2016). Partial melts obtained from dehydration melting of mafic rocks at moderate to low pressures exhibit mildly peraluminous to metaluminous melt poor in CaO and $Al_2O_3$, with relatively high in iron (Beard and Lofgren, 1991). In the $Al_2O_3$, CaO, and $Fe_2O_3^T$ vs. $SiO_2$ diagrams (Fig. 5b, d and e), the Gajin granite samples plot within or near the field of melt produced by of dehydration melting.

For the Gajin granites, the prevailing temperatures during partial melting were inferred from whole-rock zircon saturation temperatures (Watson and Harrison, 1983) and range from 746 to 831 °C. This temperature range largely agrees with the temperatures calculated from Ti saturation in zircons (~650–880 °C) (Ferry and Watson, 2007). These ranges overlap with those estimated for the Himalayan leucogranites (760 ± 25 °C, e.g., Zhang et al., 2004) and with the experimental run temperatures of fluid-absent melting of metapelites (Patiño Douce and Beard, 1995). At comparable $SiO_2$ contents, the Gajin granites have $Fe_2O_3^T$ contents similar to those of the fractionated Mianning riebeckite-bearing A-type granites (Huang et al., 2008), implying high magma temperatures for the Gajin granites. The distinctive seagull-shaped REE patterns (Fig. 6) are similar to those of rocks generated from hot and dry magmas (Bachmann and Bergantz, 2008). Melts produced by the flushing of monzogranites/granodiorites, orthogneisses, and granulite-facies felsic meta-igneous crustal lithologies are likely to be relatively dry (Holtz, 1989). The weakly peraluminous Gajin granites are distinct from typical leucogranites found elsewhere. This feature is similar to some highly evolved I-type granites (e.g., Guo et al., 2012), which indicates a mantle component or juvenile crustal material in the genesis of the Gajin granites (Kemp et al., 2007).

Considering the Early Cretaceous magma pulse in the north-central Lhasa Terrane, the scarcity of roughly coeval magmatism, and the rapid uplifting and cooling around the Early–Late Cretaceous boundary (Kapp et al., 2007; Volkmer et al., 2014), we suggest that the heat required for partial melting of the medium-lower crust was provided by underplating basaltic magmas or underlying hot lithospheric mantle (Wang et al., 2012). Thermal modeling in combination with experimental studies (Thompson and Connolly, 1995) has revealed that without the incursion of mantle heat, the dehydration melting of continental crust will not occur, even in an extensional setting. The direct incorporation of mantle-derived magmas is not applicable in the case of the Gajin granites. In addition, the possible upwelling of asthenosphere result from the delamination of lower lithospheric mantle seems to lack corroboration, as no quasi-instantaneous mantle-derived hot or magnesian-enrichment magma product have been identified in or near the study area. Heat accumulation related to faults activity could not have caused the formation of the Gajin granites because faulting occurred after the granite was intruded (Fig. 1b). Enriched felsic intrusives with highly radioactive elements have little influence on temperatures in the deep crust (Jaupart et al., 2016).

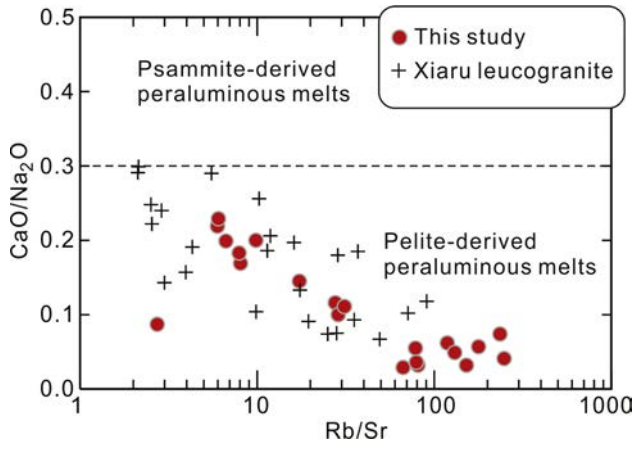


**Fig. 12.** $CaO/Na_2O$ vs. Rb/Sr plot for the Gajin granites (after Sylvester, 1998). Data for the Xiaru leucogranites in the Himalayan are from Liu et al. (2016).

Dehydration melting prevails during the melting of continental crust (Clemens and Vielzeuf, 1987; Thompson and Connolly, 1995) and may have been the main mechanism for the generating the Gajin granitic magmas. The low modal proportions of mafic phases in the Gajin granites offer additional evidence for relatively water-poor parental magmas (e.g., Frost et al., 2016). Water-fluxed melting would cause large amount of plagioclases to break down resulting in high CaO, $Al_2O_3$, and Sr contents in the derivative magma (Weinberg and Hasalová, 2015). The low content of these components of the Gajin granitic magmas are consistent with the dehydration melting of the continental crust. The strong positive correlation between Ba and Rb/Sr is similar to that expected for melt derived by fluid-absent melting (Wang et al., 2012; Zhang et al., 2004), and the low Sr/Ba ratios imply the involvement of biotite dehydration under water-undersaturated conditions (Harris and Inger, 1992). Plagioclases, K-feldspars, and some biotites are possible residual phases after partial melting, but garnets are not required (e.g., Wang et al., 2012; Zhang et al., 2004).

Based on the above discussion, a preferred petrogenetic model for the Gajin granites is as follows: dehydration melting of fertile mature continental crust materials produced the magmas that subsequently solidified to form the Gajin granites. Those materials were likely incorporated into the melting region under progressively thickening crust (Chen et al., 2015; Wang et al., 2014a) during continental collision and crust convergence.

### 6.2. Cretaceous magmatism in the north-Central Lhasa Terrane

A magmatic lull from ~100 to 85 Ma following the late Early Cretaceous magma peak has been revealed (Fig. 13). The extensive and voluminous Early Cretaceous magmatism (~103–105 Ma) in the north-central Lhasa Terrane (Zhu et al., 2016) are dominated by silicic to intermediate, medium- to high-K calc-alkaline series, with rare mafic rocks (Zhu et al., 2016, and references therein). There was a pronounced magma flare up from ~130 to 105 Ma (Fig. 13). A period of magmatic quiescence from ~100 to 85 Ma following the Early Cretaceous peak can be identified in the north-central Lhasa Terrane. After this lull, the Late Cretaceous intrusive or extrusive eruptions were limited in both volume and spatial distribution.

There is a clear difference between the rock compositions and assemblages formed prior to the early Late Cretaceous magmatic lull and those formed afterward (Fig. 14), indicating a spatial–temporal evolution in the rock association and the mechanism of magma production. Although the Early Cretaceous magmatic activity shows geochemical diversity, it was dominated by the production of calc-alkaline granitoids and ended with the emplacement of the monotonous high-silica granites of this study. In contrast, the ~80–90 Ma magmatic rocks in the north-central Lhasa Terrane are limited in volumes but exhibit high proportions of mantle-derived melts (with high Mg#, high Cr concentration, and strong mantle-derived melts signals), and shows geochemical features (with the basaltic rocks having high Zr concentrations and high Zr/Y ratios) similar to those of an intra-plate magma (Wang et al., 2014a, and references therein).

A systematic variation in source characteristics has also been revealed by whole-rock Nd and zircon Hf isotopes (145 published Nd and >1400 zircon Hf data) from the north-central Lhasa Terrane (Fig. 15). From the Jurassic to the Early Cretaceous (~130 Ma), the contribution of ancient crust prevailed and was maintained at a fairly constant level, accompanied by a gradual increase in mantle-derived components. The contribution of depleted mantle increased substantially during the late Early Cretaceous magmatic flare-up. In contrast, the isotopic signatures of the Late Cretaceous magmatic rocks point to the coeval involvement of mantle sources and to the recycling of ancient continental crust (Fig. 15).

The magmatic gap from ~100 to 85 Ma can not be interpreted satisfactorily by flat-slab subduction because there is no reliable evidence for the migration of magmatic arc fronts and foreland basin depocenters towards the continental interior (e.g., Li and Li, 2007; Ramos and Folguera, 2009). Alternatively, continental collision is a simple and reasonable

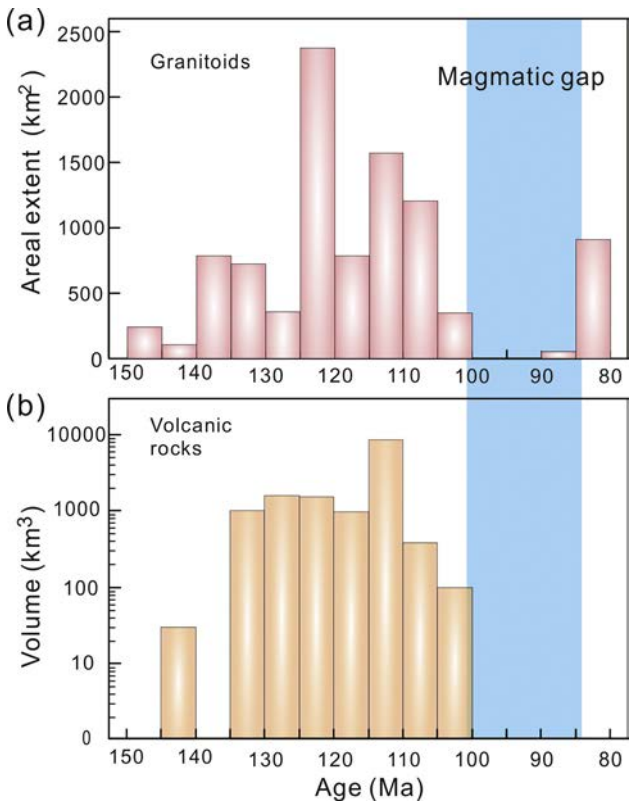


**Fig. 13.** Histograms of the areal extent of granitic rocks (a) and the volume of volcanic rocks (b) in the north-central Lhasa Terrane. The data for the volcanic rocks are from Kang et al. (2008), Zhu et al. (2016) and references therein. The data for granitoids are from Chen et al. (2015), Volkmer et al. (2014), Wu et al. (2015), and Zhu et al. (2016) and references therein.

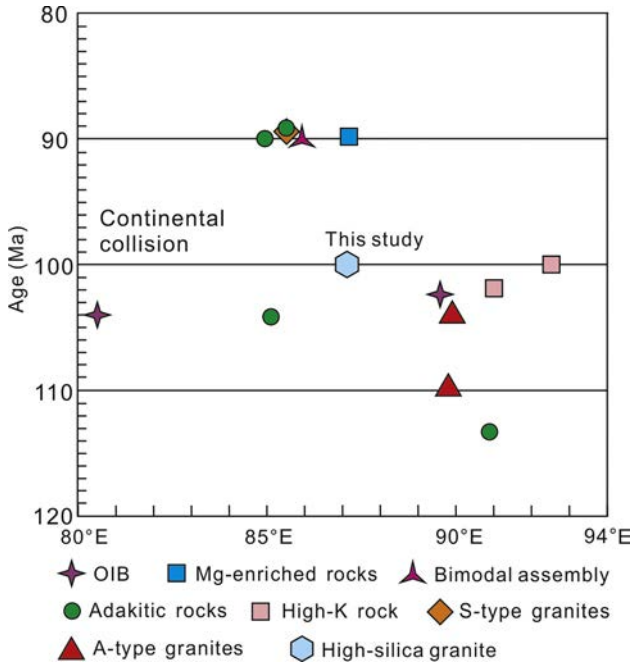


**Fig. 14.** Spatial–temporal changes of rock associations of the north-central Lhasa Terrane. Data are from Chen et al. (2014b), Chen et al. (2015), Liu et al. (2014), Qu et al. (2012), Sun et al. (2015), Wang et al. (2014a), Wu et al. (2015), and Zhu et al. (2016).

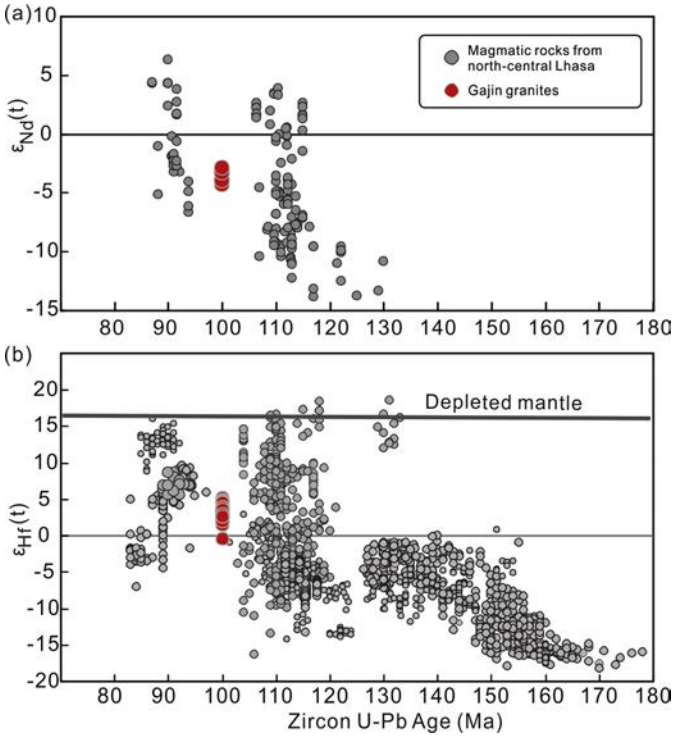


**Fig. 15.** Whole-rock Nd (a) and zircon Hf isotopic values (b) of igneous rocks in the north-central Lhasa Terrane. Whole-rock Nd isotope data are from Chen et al. (2015), Chen et al. (2017a), Qu et al. (2012), Wang et al. (2014), Zhu et al. (2016); The Hf isotope data are from Chen et al. (2017a), Li et al. (2017a), Sun et al. (2015), Wang et al. (2014), Wu et al. (2015), Zhu et al. (2016) and references therein.

explanation of the development of the magmatic gap (Condie et al., 2009). The detailed evidence for this is discussed in the following section.

### 6.3. Continental collision at ~100 Ma

The timing of continental collision between the Lhasa and Qiangtang Terranes remians contentious, with previous studies proposing the Mid-Jurassic (Ma et al., 2017a), Late Jurassic (Li et al., 2017b; Zhu et al., 2016), Early Cretaceous (Hao et al., 2016, 2018), and Late Cretaceous (Zhang et al., 2012). Although time of initial collision is difficult to constrain, multiple geological observations collectively indicate that the collision between the Qiangtang and Lhasa terranes likely began no later than ~100 Ma (He et al., 2018).

An angular unconformity that separates the upper Bathonian to lower Callovian fan-delta conglomerates and sandstone from underlying shallow-marine limestone and sandstones of the southern Qiangtang Terrane has been dated at ~166 Ma (Ma et al., 2017a). This unconformity has been ascribed to the continental collision between the Qiangtang and Lhasa terranes; however, the conglomerates above the unconformity have a thickness of <300 m, reducing to <50 m less than ~15 km south of the measured section (Ma et al., 2017a). More importantly, the sequences below and above this surface are both characterized by a delta + carbonate-platform association, and there is no evidence for significant parts of this stratigraphic sequence having been removed at ~166 Ma. Therefore, the stratigraphic unconformity (Ma et al., 2017a) most likely resulted from local crustal uplift that may have been related to arc–continent collision (Fan et al., 2018, and references therein). The Middle Jurassic collision scenario is inconsistent with the late Hauterivian–early Aptian radiolaria recorded in chert and siliceous mudstones from the Lagkor Tso ophiolitic mélange (Baxter et al., 2009), which is part of the BNSZ or relict back-arc basin related to underthrusting by oceanic lithospheric (Wang et al., 2016).

Basaltic rocks within the BNSZ exhibiting a geochemical affinity for ocean island basalt yield ages as young as 120–110 Ma (Fan et al., 2018, and references therein; Wang et al., 2016; Zhu et al., 2016, and references therein). Pillow basalts within the BNSZ that yield an age of ~104 Ma show island-arc and MORB tholeiite affinities (Liu et al., 2014), implying that this ocean was still open during the mid-Cretaceous. These data indicate that the closure of the ocean, as represented by the development of the BNSZ, did not take place until ~110 Ma (Hao et al., 2016, 2018).

However, the time of collision between the Lhasa and Qiangtang terranes has previously been placed at ~140 Ma (Zhu et al., 2016, and references therein) on the basis of 1) an angular unconformity at ~145 Ma, 2) the scarcity of 140–130 Ma magmatic rocks in the southern Qiangtang Terrane, and 3) the presence of ~114 Ma A-type granitic rocks in the northern Lhasa Terrane (Chen et al., 2014b). However, the geological dynamics with aspect to this angular unconformity are ambiguous and might not be associated with continental collision. Sedimentary rocks deposited both below and above the ~145 Ma unconformity are sandstones (e.g., Zhu et al., 2016) but without the coarse-grained conglomerates that are typically related to collisional event, and the angular unconformity is restricted to the northern margin of the BNSZ (Fan et al., 2018).

The magmatic gap with age between 140 and 130 Ma has been interpreted by in terms of oceanic plateau subduction (e.g., Hao et al., 2018). If this magmatic gap in the southern Qiangtang Terrane had resulted from collision, it would be difficult to reconcile the volcano-plutonic activity that continued to occur widely across the Lhasa Terrane (Fig. 13).

Geological mapping and geochronological data of the Coqen and Nyima area reveal a significant crustal shortening and regional uplifting during the Cretaceous (Kapp et al., 2007) as a result of collision between the Lhasa and Qiangtang Terranes. The limited heat source from the deep mantle and the regional compression caused by the continental collision (Nabelek and Liu, 2004) together resulted in the paucity of collision-related magma activity.

The magmatic quiescence during the earliest Late Cretaceous is largely coeval with continental compression and crustal uplift. In the Nyima basin, ~50 km north of the study area, a transformation from marine facies to terrestrial deposits was recorded in the Cretaceous sedimentary succession near the Early–Late Cretaceous boundary (~115–100 Ma) (Fig. 4 in Kapp et al., 2007). A sequence of volcanoclastic conglomerates and limestone-clast conglomerates, with a total thickness of >1500 m, showing thickening and coarsening upward profile, overlies the Early Cretaceous marine fine-grained sandstone and is in turn overlain by lacustrine deposits above an angular unconformity (Kapp et al., 2007). A similar transition from marine to nonmarine sedimentation, occurring at ~104 Ma, has also been observed in the Xiagangjiang Range area, central Lhasa Terrane (Volkmer et al., 2014, and references therein).

The Jingzhushan Formation conglomerates are distributed along the BNSZ, overlying the Early Cretaceous succession above an angular unconformity. This formation has been suggested to comprise terrigenous molasses that recorded the collision between the Qiangtang and Lhasa terranes (Pan et al., 2012; Zhang et al., 2012). Cenomanian fossils including *Neonerinea* cf. *ferganensis* (Pchelincev) and *Orbitolina concava* have been identified from this formation. The sediments of this formation were sourced from the Lhasa and Qiangtang terranes and the intervening suture zone, with the youngest detrital zircons having ages ranging from ~91 to 79 Ma (Li et al., 2017b). The Abushan Formation alluvial-lacustrine facies sediments in the southern Qiangtang Terrane are the chronostratigraphic equivalent of the Jingzhushan Formation (e.g., Zhang et al., 2012; Zhu et al., 2016). Volcanic rocks and detrital zircons from the Abushan Formation yield zircon crystallization ages and youngest age peak of ~100 Ma, respectively (Li et al., 2015; Ma et al., 2017a), which are broadly consistent with the age of the Jingzhushan Formation and the emplacement of the Gajin granites. These geological

observations collectively suggest a ~100 Ma tectonic compression and regional crustal uplift that likely resulted from continental collision between the Qiangtang and Lhasa terranes.

Importantly, the rapid cooling from ~110 to 105 Ma recorded by the Xiabie granites indicates a coincidental rapid crustal uplift (Kapp et al., 2007). About 200 km east of Nyima, the Baingoin plutonic complex also records a slightly later rapid cooling event from ~105 to 95 Ma (Volkmer et al., 2014).

Recently obtained paleomagnetic data on the Early Cretaceous volcanic rocks (~120 Ma) from the northern margin of the Lhasa Terrane (Li et al. 2017b; Ma et al., 2017c) and on the ~104 Ma volcanic rocks from South Qiangtang (Chen et al., 2017b) suggest that the Lhasa and Qiangtang Terranes were located at a constant paleolatitude and that they occupied an indistinguishable space (e.g., Ma et al., 2017c), implying that the amalgamation between these two terranes was completed no later than ~100 Ma.

Independent multidisciplinary observations suggest that the emplacement of the Gajin granites was coeval with a tectonic compression and crustal uplift event that occurred from ~110 to 90 Ma. These data, in combination with the 105–85 Ma magmatic gap in the north-central Lhasa Terrane (Fig. 13), suggest that the continental collision between the Lhasa and Qiangtang terranes started no later than ~100 Ma (e.g., He et al., 2018; Liu et al., 2018).

### 6.4. Geological implications

High-silica granites can be divided into two groups that form in contrasting tectonic environments: one in association with continental arcs, and the other in association with continental collisional orogeny. Continental arcs are generally dominated by large felsic batholiths, and show a wide range of rock types, from gabbros to diorites, to quartzdiorites, and to some true granites but they are dominated by granodiorites (e.g., Chung et al., 2005; Lee et al., 2007). This wide range of rock composition is typical of the west coast North and South America (Hervé et al., 2007; Lipman, 2007), and the late Mesozoic Gangdese magmatic arc in Tibet (Chung et al., 2005). In contrast, drastically reduced magmatism is a characteristic feature of continental collision, and magmatic products are dominated by sparse plutons with uniform compositions, with the proportions of magma derived from mantle decreased sharply. An end-member case is the Himalayan leucogranites (Liu et al., 2016; Ma et al., 2017b; Zhang et al., 2004).

A distinction between arc- and collision-related high-silica granites can be found in their rock associations: arc-related granites have a genetic relationship with more mafic variations from diorites to granodiorites, whereas, collision-related granites are chemically monotonous. Arc-related high-silica granites show a wide range of silica contents, suggesting the importance of fractional crystallization (Lee et al., 2007; Lee and Morton, 2015), whereas, the high-silica granites from collision-related environments (e.g., the Himalayan leucogranites) have more restricted ranges of silica contents and show relatively homogeneous major element compositions (Le Fort, 1981), indicating the dominance of the partial melting of crustal materials (Frost et al., 2016). Such a fundamental difference may result from the different thermal configurations related to the contrasting geodynamic processes operating in arc and collision setting.

Insights into such thermal configurations have been gained by investigations of the late Archean high-silica granites from old continental crusts. High-silica granites are characteristic of late Archean continental crust (Laurent et al., 2014; Moyen et al., 2003), and the generation of such granites has been explained in terms of a fundamental change in heat attenuation (Bagdnoas et al., 2016; Laurent et al., 2014). The change in rock compositions from continental arc-related granites with a wide range of silica contents to collision-related granites with uniformly high silica content could be attributed to a change in heat conditions associated with geodynamic changes during the transition between tectonic regimes. The huge volumes of igneous rocks (e.g., the Gangdese batholiths and Linzizong volcanic rocks, Chung et al., 2005) from a continental arc reflect the high heat flux from the convective mantle. In contrast, the relatively small volumes and monotonous high-silica granites in collisional setting reflects the limited heat available for crustal melting during or after the collision (Nabelek and Liu, 2004; Zhang et al., 2004). Furthermore, late Archean high-silica granites were typically intruded into widely distributed tonalite-trondhjemite-granodiorite or “gray gneisses” and were generally followed by a magmatic shutdown (Condie et al., 2009).

A similar mechanism may have been responsible for the development of the Gajin high-silica granites. These granites were intruded after the Early Cretaceous magma peak of the Lhasa Terrane, and their emplacement was followed by a magmatic lull (Fig. 13). High-silica granites from the Herberton mineral field, Australia (Cheng et al., 2018), Late Cretaceous Xiuwacu granites from the Yidun Terrane, eastern Tibet (Wang et al., 2014b), and the ~43 Ma Dajia granites in the western Gangdese, southern Tibet (Wang et al., 2015) were all emplaced during times of tectonic changes. Thermal attenuation related to geodynamic changes (Condie et al., 2009; Laurent et al., 2014) may be the underlying mechanism generating these distinct and monotonous high-silica granites. Such granites may be more common than previously recognized and represent the important yet under-evaluated magma products of continental collision dynamics.

## 7. Conclusions

(1) Geochemical and zircon U—Pb dating results suggest that the Gajin plutons are high-silica granites that formed at ~100 Ma.
(2) Whole-rock geochemistry and Nd isotopes and zircon Hf isotope compositions indicate that the Gajin granites are highly evolved rocks that resulted from the extensive fractional crystallizations of magmas derived from the middle–lower continental crust.
(3) Other geological observations (e.g., the presence of a regional angular unconformity and a magmatic lull from ~100 to 85 Ma) suggest that the Gajin granites were emplaced no later than the beginning of the continental collision between the Lhasa and Qiangtang Terranes.
(4) The generation of monotonous high-silica granites can be explained in terms of the geodynamic processes operating during a regional tectono-thermal transition.

Supplementary data to this article can be found online at https://doi.org/10.1016/j.lithos.2018.11.011.

## Acknowledgments

We sincerely thank Editor-in-Chief Dr. Andrew Kerr and two anonymous reviewers for their constructive and helpful reviews and suggestions. We are grateful to Yang Yueheng, Liu Xijun, and Zhang Le for their assistance with zircon isotopic analyses. We would like to thank Liu Yin, Tu Xiangling, Sun Shengling, and Zeng Wen for their help with whole-rock chemical analyses. This study was jointly supported by the National Key R & D Program of China (2016YFC0600407), the Strategic Priority Research Program (A) of the Chinese Academy of Sciences (No. XDA2007030402), the Key Program of the Chinese Academy of Sciences (QYZDJ–SSW–DQC026), the National Natural Science Foundation of China (grant no. 41630208), the Strategic Priority Research Program (A) of the Chinese Academy of Sciences (No. XDA2007030402), the Key Science Program of Guangzhou City (201707020032), and the Guangzhou Institute of Geochemistry, Chinese Academy of Sciences (GIGCAS 135 Project [135TP201601]). This is contribution No.IS-2610 from GIG-CAS.

## References


Bachmann, O., Bergantz, G.W., 2008. Rhyolites and their source mushes across tectonic settings. J. Petrol. 49, 2277–2285.

Bagdonas, D.A., Frost, C.D., Fanning, C.M., 2016. The origin of extensive Neoarchean high-silica batholiths and the nature of intrusive complements to silicic ignimbrites: insights from the Wyoming batholith, U.S.a. Am. Mineral. 101, 1321–1331.

Baker, D.R., Vaillancourt, J., 1995. The low viscosities of F + H2O-bearing granitic melts and implications for melt extraction and transport. Earth Planet. Sci. Lett. 132, 199–211.

Ballouard, C., Poujol, M., Boulvais, P., Branquet, Y., Tartèse, R., Vigneresse, J.L., 2016. Nb-Ta fractionation in peraluminous granites: a marker of the magmatic-hydrothermal transition. Geology 44, 231–234.

Baxter, A.T., Aitchison, J.C., Zyabrev, S.V., 2009. Radiolarian age constraints on Mesotethyan ocean evolution, and their implications for development of the Bangong–Nujiang suture, Tibet. Journal of the Geological Society 166, 689–694.

Beard, J.S., Lofgren, G.E., 1991. Dehydration melting and water-saturated melting of basaltic and andesitic greenstones and amphibolites at 1, 3, and 6. 9 kb. J. Petrol. 32, 465–501.

Black, L.P., Kamo, S.L., Allen, C.M., Aleinikoff, J.N., Davis, D.W., Korsch, R.J., Foudoulis, C., 2003. TEMORA 1: a new zircon standard for Phanerozoic U–Pb geochronology. Chem. Geol. 200, 155–170.

Chen, B., Ma, X., Wang, Z., 2014a. Origin of the fluorine-rich highly differentiated granites from the Qianlishan composite plutons (South China) and implications for polymetallic mineralization. J. Asian Earth Sci. 93, 301–314.

Chen, Y., Zhu, D.-C., Zhao, Z.-D., Meng, F.-Y., Wang, Q., Santosh, M., Wang, L.-Q., Dong, G.-C., Mo, X.-X., 2014b. Slab breakoff triggered ca. 113 Ma magmatism around Xainza area of the Lhasa Terrane, Tibet. Gondwana Res. 26, 449–463.

Chen, J.-L., Xu, J.-F., Yu, H.-X., Wang, B.-D., Wu, J.-B., Feng, Y.-X., 2015. Late cretaceous high-Mg# granitoids in southern Tibet: Implications for the early crustal thickening and tectonic evolution of the Tibetan Plateau? Lithos 232, 12–22.

Chen, S.-S., Shi, R.-D., Gong, X.-H., Liu, D.-L., Huang, Q.-S., Yi, G.-D., Wu, K., Zou, H.-B., 2017a. A syn-collisional model for early cretaceous magmatism in the northern and Central Lhasa subterranes. Gondwana Res. 41, 93–109.

Chen, W., Zhang, S., Ding, J., Zhang, J., Zhao, X., Zhu, L., Yang, W., Yang, T., Li, H., Wu, H., 2017b. Combined paleomagnetic and geochronological study on cretaceous strata of the Qiangtang terrane, Central Tibet. Gondwana Res. 41, 373–389.

Cheng, Y., Spandler, C., Chang, Z., Clarke, G., 2018. Volcanic–plutonic connections and metal fertility of highly evolved magma systems: a case study from the Herberton Sn–W–Mo Mineral Field, Queensland, Australia. Earth Planet. Sci. Lett. 486, 84–93.

Chung, S.-L., Chu, M.-F., Zhang, Y., Xie, Y., Lo, C.-H., Lee, T.-Y., Lan, C.-Y., Li, X., Zhang, Q., Wang, Y., 2005. Tibetan tectonic evolution inferred from spatial and temporal variations in post-collisional magmatism. Earth-Sci. Rev. 68, 173–196.

Clemens, J., Vielzeuf, D., 1987. Constraints on melting and magma production in the crust. Earth Planet. Sci. Lett. 86, 287–306.

Condie, K.C., O'Neill, C., Aster, R.C., 2009. Evidence and implications for a widespread magmatic shutdown for 250 my on Earth. Earth Planet. Sci. Lett. 282, 294–298.

Eby, G.N., 1990. The A-type granitoids: a review of their occurrence and chemical characteristics and speculations on their petrogenesis. Lithos 26, 115–134.

Fan, J.J., Li, C., Xie, C.M., Wang, M., Chen, J.W., 2018. Reconstructing in space and time the closure of the middle and western segments of the Bangong-Nujiang Tethyan Ocean in the Tibetan Plateau. Int. J. Earth Sci. (Geol. Rundsch.) 107, 231–249.

Ferry, J., Watson, E., 2007. New thermodynamic models and revised calibrations for the Ti-in-zircon and Zr-in-rutile thermometers. Contrib. Mineral. Petrol. 154 (4), 429–437.

Frost, C.D., Swapp, S.M., Frost, B.R., Finley-Blasi, L., Fitz-Gerald, D.B., 2016. Leucogranites of the Teton Range, Wyoming: a record of archean collisional orogeny. Geochim. Cosmochim. Acta 185, 528–549.

Gelman, S.E., Deering, C.D., Bachmann, O., Huber, C., Gutiérrez, F.J., 2014. Identifying the crystal graveyards remaining after large silicic eruptions. Earth Planet. Sci. Lett. 403, 299–306.

Giordano, D., Romano, C., Dingwell, D.B., Poe, B., Behrens, H., 2004. The combined effects of water and fluorine on the viscosity of silicic magmas. Geochim. Cosmochim. Acta 68, 5159–5168.

Green, T.H., 1995. Significance of Nb/Ta as an indicator of geochemical processes in the crust-mantle system. Chem. Geol. 120, 347–359.

Guo, C., Chen, Y., Zeng, Z., Lou, F., 2012. Petrogenesis of the Xihuashan granites in southeastern China: constraints from geochemistry and in-situ analyses of zircon U Pb Hf O isotopes. Lithos 148, 209–227.

Gu, L.-x., Zhang, Z.-z., Wu, C.-z., Liao, J.-j., Yang, H., 2011. A topaz-and amazonite-bearing leucogranite pluton in eastern Xinjiang, NW China and its zonin. Journal of Asian Earth Sciences 42, 885–902.

Hao, L.-L., Wang, Q., Wyman, D.A., Ou, Q., Dan, W., Jiang, Z.-Q., Wu, F.-Y., Yang, J.-H., Long, X.-P., Li, J., 2016. Underplating of basaltic magmas and crustal growth in a continental arc: evidence from late Mesozoic intermediate–felsic intrusive rocks in southern Qiangtang, Central Tibet. Lithos 245, 223–242.

Hao, L.-L., Wang, Q., Zhang, C., Ou, Q., Yang, J.-H., Dan, W., Jiang, Z.-Q., 2018. Oceanic plateau subduction during closure of Bangong-Nujiang Tethys: insights from Central Tibetan volcanic rocks. Geol. Soc. Am. Bull. 120. https://doi.org/10.1130/B32045.1.

Harris, N.B.W., Inger, S., 1992. Trace element modelling of pelite-derived granites. Contrib. Mineral. Petrol. 110, 46–56.

He, H., Li, Y., Wang, C., Zhou, A., Qian, X., Zhang, J., Du, L., Bi, W., 2018. Late cretaceous (ca. 95 Ma) magnesian andesites in the Biluoco area, southern Qiangtang subterrane, Central Tibet: petrogenetic and tectonic implications. Lithos 302-303, 389–404.

Hervé, F., Pankhurst, R.J., Fanning, C.M., Calderón, M., Yaxley, G.M., 2007. The south Patagonian batholith: 150my of granite magmatism on a plate margin. Lithos 97, 373–394.

Holtz, F., 1989. Importance of melt fraction and source rock composition in crustal genesis — the example of two granitic suites of northern Portugal. Lithos 24, 21–35.

Hu, D., Wu, Z., Jiang, W., Shi, Y., Ye, P., Liu, Q., 2005. SHRIMP zircon U-Pb age and Nd isotopic study on the Nyainqêntanglha Group in Tibet. Sci. China Ser. D Earth Sci. 48, 1377.

Huang, X.L., Xu, Y.G., Li, X.H., Li, W.X., Lan, J.B., Zhang, H.H., Liu, Y.S., Wang, Y.B., Li, H.Y., Luo, Z.Y., 2008. Petrogenesis and tectonic implications of Neoproterozoic, highly fractionated A-type granites from Mianning, South China. Precambrian Res. 165, 190–204.

Jaupart, C., Mareschal, J.-C., Iarotsky, L., 2016. Radiogenic heat production in the continental crust. Lithos 262, 398–427.

Jiang, Z.-Q., Wang, Q., Li, Z.-X., Wyman, D.A., Tang, G.-J., Jia, X.-H., Yang, Y.-H., 2012. Late cretaceous (ca. 90Ma) adakitic intrusive rocks in the Kelu area, Gangdese Belt (southern Tibet): Slab melting and implications for Cu–au mineralization. J. Asian Earth Sci. 53, 67–81.

Jung, S., Mezger, K., Nebel, O., Kooijman, E., Berndt, J., Hauff, F., Münker, C., 2012. Origin of Meso-Proterozoic post-collisional leucogranite suites (Kaokoveld, Namibia): constraints from geochronology and Nd, Sr, Hf, and Pb isotopes. Contrib. Mineral. Petrol. 163, 1–17.

Kapp, P., Decelles, P.G., Gehrels, G.E., Heizler, M., Ding, L., 2007. Geological records of the Lhasa-Qiangtang and Indo-Asian collisions in the Nima area of Central Tibet. Geol. Soc. Am. Bull. 119, 917–933.

Kemp, A.I.S., Hawkesworth, C.J., Foster, G.L., et al., 2007. Magmatic and crustal differentiation history of granitic rocks from Hf-O isotopes in zircon. Science 315, 980–983.

Laurent, O., Martin, H., Moyen, J.F., Doucelance, R., 2014. The diversity and evolution of late-Archean granitoids: evidence for the onset of "modern-style" plate tectonics between 3.0 and 2.5 Ga. Lithos 205, 208–235.

Le Fort, P., 1981. Manaslu leucogranite: a collision signature of the Himalaya: a model for its genesis and emplacement. J. Geophys. Res. Solid Earth 86, 10545–10568.

Lee, C.-T.A., Morton, D.M., 2015. High silica granites: terminal porosity and crystal settling in shallow magma chambers. Earth Planet. Sci. Lett. 409, 23–31.

Lee, C.T.A., Morton, D.M., Kistler, R.W., Baird, A.K., 2007. Petrology and tectonics of Phanerozoic continent formation: from island arcs to accretion and continental arc magmatism. Earth Planet. Sci. Lett. 263, 370–387.

Li, Z., Li, X., 2007. Formation of the 1300-km-wide intracontinental orogen and postorogenic magmatic province in Mesozoic South China: a flat-slab subduction model. Geology 35, 179–182.

Li, X.-H., Li, Z.-X., Wingate, M.T.D., Chung, S.-L., Liu, Y., Lin, G.-C., Li, W.-X., 2006. Geochemistry of the 755 Ma Mundine well dyke swarm, northwestern Australia: part of a Neoproterozoic mantle superplume beneath Rodinia? Precambrian Res. 146, 1–15.

Li, Y., He, J., Wang, C., Han, Z., Ma, P., Xu, M., Du, K., 2015. Cretaceous volcanic rocks in south Qiangtang Terrane: Products of northward subduction of the Bangong–Nujiang Ocean? Journal of Asian Earth Sciences 104, 69–83.

Li, G.-M., Qin, K.-Z., Li, J.-X., Evans, N.J., Zhao, J.-X., Cao, M.-J., Zhang, X.-N., 2017a. Cretaceous magmatism and metallogeny in the Bangong–Nujiang metallogenic belt, Central Tibet: evidence from petrogeochemistry, zircon U–Pb ages, and Hf–O isotopic compositions. Gondwana Res. 41, 110–127.

Li, S., Guilmette, C., Ding, L., Xu, Q., Fu, J.-J., Yue, Y.-H., 2017b. Provenance of mesozoic clastic rocks within the Bangong-Nujiang suture zone, Central Tibet: implications for the age of the initial Lhasa-Qiangtang collision. J. Asian Earth Sci. 147, 469–484.

Linnen, R.L., Keppler, H., 2002. Melt composition control of Zr/Hf fractionation in magmatic processes. Geochim. Cosmochim. Acta 66, 3293–3301.

Lipman, P.W., 2007. Incremental assembly and prolonged consolidation of Cordilleran magma chambers: evidence from the Southern Rocky Mountain volcanic field. Geosphere 3, 42–70.

Liu, Y.S., Zong, K.Q., Kelemen, P.B., Gao, S., 2008. Geochemistry and magmatic history of eclogites and ultramafic rocks from the Chinese continental scientific drill hole: Subduction and ultrahigh-pressure metamorphism of lower crustal cumulates. Chem. Geol. 247, 133–153.

Liu, W.L., Xia, B., Zhong, Y., Cai, J.X., Li, J.F., Liu, H.F., Cai, Z.R., Sun, Z.L., 2014. Age and composition of the Rebang Co and Julu ophiolites, Central Tibet: implications for the evolution of the Bangong Meso-Tethys. Int. Geol. Rev. 56, 430–447.

Liu, Z.-C., Wu, F.-Y., Ding, L., Liu, X.-C., Wang, J.-G., Ji, W.-Q., 2016. Highly fractionated late Eocene (~ 35 Ma) leucogranite in the Xiaru Dome, Tethyan Himalaya, South Tibet. Lithos 240–243, 337–354.

Liu, D.-L., Shi, R.-D., Ding, L., Zou, H.-B., 2018. Late cretaceous transition from subduction to collision along the Bangong-Nujiang Tethys: new volcanic constraints from Central Tibet. Lithos 296-299, 452–470.

Ludwig, K.R., 2003. User's Manual for Isoplot 3.0: a Geochronological Toolkit for Microsoft Excel. vol. 4. Berkeley Geochronology Center. Special Publication., pp. 1–71.

Ma, A., Hu, X., Garzanti, E., Han, Z., Lai, W., 2017a. Sedimentary and tectonic evolution of the southern Qiangtang basin: implications for the Lhasa-Qiangtang collision timing: Mesozoic geology of Central Tibet. J. Geophys. Res. Solid Earth 122, 4790–4813.

Ma, L., Wang, Q., Kerr, A.C., Yang, J.-H., Xia, X.-P., Quan, O., Yang, Z.-Y., Sun, P., 2017b. Paleocene (c. 62 Ma) Leucogranites in Southern Lhasa, Tibet: products of syn-collisional crustal anatexis during slab roll-back? J. Petrol. 58, 2089–2114.

Ma, Y., Yang, T., Bian, W., Jin, J., Wang, Q., Zhang, S., Wu, H., Li, H., Cao, L., Yuan, H., Ding, J., 2017c. Paleomagnetic and geochronologic results of latest cretaceous lava flows from the Lhasa terrane and their tectonic implications. J. Geophys. Res. Solid Earth 122, 8786–8809.

Mackenzie, D.E., Black, L.P., Sun, S.-S., 1988. Origin of alkali-feldspar granites: an example from the Poimena Granite, northeastern Tasmania, Australia. Geochim. Cosmochim. Acta 52, 2507–2524.

Marini, J.C., Chauvel, C., Maury, R.C., 2005. Hf isotope compositions of northern Luzon arc lavas suggest involvement of pelagic sediments in their source. Contrib. Mineral. Petrol. 149, 216–232.
Morel, M.L.A., Nebel, O., Nebel-Jacobsen, Y.J., Miller, J.S., Vroon, P.Z., 2008. Hafnium isotope characterization of the GJ-1 zircon reference material by solution and laser-ablation MC-ICPMS. Chem. Geol. 255, 231–235.
Moyen, J.F., Martin, H., Jayananda, M., Auvray, B., 2003. Late Archaean granites: a typology based on the Dharwar Craton (India). Precambrian Res. 127, 103–123.
Nabelek, P.I., Liu, M., 2004. Petrologic and thermal constraints on the origin of leucogranites in collisional orogens. Trans. R. Soc. Edinb. Earth Sci. 95, 73–85.
Ou, Q., Wang, Q., Wyman, D.A., Zhang, H.X., Yang, J.H., Zeng, J.P., Hao, L.L., Chen, Y.W., Liang, H., Qi, Y., 2017. Eocene adakitic porphyries in the central-northern Qiangtang Block, Central Tibet: partial melting of thickened lower crust and implications for initial surface uplifting of the plateau. J. Geophys. Res. Solid Earth 122.
Pan, G., Wang, L., Li, R., Yuan, S., Ji, W., Yin, F., Zhang, W., Wang, B., 2012. Tectonic evolution of the Qinghai-Tibet Plateau. J. Asian Earth Sci. 53, 3–14.
Patiño Douce, A.E., Beard, J.S., 1995. Dehydration-melting of biotite gneiss and quartz amphibolite from 3 to 15 kbar. J. Petrol. 36, 707–738.
Qu, X.-M., Wang, R.-J., Xin, H.-B., Jiang, J.-H., Chen, H., 2012. Age and petrogenesis of A-type granites in the middle segment of the Bangonghu–Nujiang suture, Tibetan plateau. Lithos 146–147, 264–275.
Ramos, V.A., Folguera, A., 2009. Andean Flat-Slab Subduction through Time. 327. Geological Society London Special Publications, pp. 31–54.
Rudnick, R.L., Gao, S., 2003. The composition of the continental crust. In: Rudnick, R.L. (Ed.), The Crust. Elsevier, Oxford, pp. 1–64.
Stepanov, A., A. Mavrogenes, J., Meffre, S., Davidson, P., 2014. The key role of mica during igneous concentration of tantalum. Contrib. Mineral. Petrol. 167, 1009.
Streckeisen, A., Le Maitre, R.W., 1979. A chemical approximation to the modal QAPF classification of the igneous rocks. Neues Jb. Mineral. Abh. 136, 169–206.
Sun, S.S., McDonough, W.S., 1989. Chemical and isotopic systematics of oceanic basalts: implications for mantle composition and processes. Geol. Soc. Lond., Spec. Publ. 42 (1), 313–345.
Sun, G.Y., Hu, X.M., Zhu, D.C., Hong, W.T., Wang, J.G., Wang, Q., 2015. Thickened juvenile lower crust-derived ~ 90 Ma adakitic rocks in the Central Lhasa terrane, Tibet. Lithos 224-225, 225–239.
Sylvester, P.J., 1998. Post-collisional strongly peraluminous granites. Lithos 45, 29–44.
Thompson, A.B., Connolly, J.A.D., 1995. Melting of the continental crust: some thermal and petrological constraints on anatexis in continental collision zones and other tectonic settings. J. Geophys. Res. Solid Earth 100, 15565–15579.
Tindle, A.G., Pearce, J.A., 1981. Petrogenetic modelling of in situ fractional crystallization in the zoned Loch Doon Pluton, Scotland. Contrib. Mineral. Petrol. 78, 196–207.
Vervoort, J.D., Plank, T., Prytulak, J., 2011. The Hf–Nd isotopic composition of marine sediments. Geochim. Cosmochim. Acta 75, 5903–5926.
Volkmer, J.E., Kapp, P., Horton, B.K., Gehrels, G.E., Minervini, J.M., Ding, L., 2014. Northern Lhasa Thrust Belt of Central Tibet: Evidence of Cretaceous–Early Cenozoic Shortening within a Passive Roof Thrust System? vol. 507. Geological Society of America, Special Paper, pp. 59–70
Wang, Q., Chung, S.L., Li, X.H., Wyman, D., Li, Z.X., Sun, W.D., Qiu, H.N., Liu, Y.S., Zhu, Y.T., 2012. Crustal melting and flow beneath Northern Tibet: evidence from mid-miocene to quaternary strongly peraluminous rhyolites in the Southern Kunlun Range. J. Petrol. 53, 2523–2566.
Wang, Q., Zhu, D.-C., Zhao, Z.-D., Liu, S.-A., Chung, S.-L., Li, S.-M., Liu, D., Dai, J.-G., Wang, L.-Q., Mo, X.-X., 2014a. Origin of the ca. 90 Ma magnesia-rich volcanic rocks in SE Nyima, Central Tibet: products of lithospheric delamination beneath the Lhasa-Qiangtang collision zone. Lithos 198–199, 24–37.
Wang, X.S., Hu, R.Z., Bi, X.W., Leng, C.B., Pan, L.C., Zhu, J.J., Chen, Y.W., 2014b. Petrogenesis of late cretaceous I-type granites in the southern Yidun Terrane: new constraints on the late Mesozoic tectonic evolution of the eastern Tibetan Plateau. Lithos 208-209, 202–219.
Wang, Q., Zhu, D.-C., Cawood, P.A., Zhao, Z.-D., Liu, S.-A., Chung, S.-L., Zhang, L.-L., Liu, D., Zheng, Y.-C., Dai, J.-G., 2015. Eocene magmatic processes and crustal thickening in southern Tibet: Insights from strongly fractionated ca. 43Ma granites in the western Gangdese Batholith. Lithos 239, 128–141.
Wang, B.-D., Wang, L.-Q., Chung, S.-L., Chen, J.-L., Yin, F.-G., Liu, H., Li, X.-B., Chen, L.-K., 2016. Evolution of the Bangong–Nujiang Tethyan Ocean: Insights from the geochronology and geochemistry of mafic rocks within ophiolites. Lithos 245, 18–33.
Watson, E.B., Harrison, T.M., 1983. Zircon saturation revisited: temperature and composition effects in a variety of crustal magma types. Earth Planet. Sci. Lett. 64, 295–304.
Weinberg, R.F., Hasalová, P., 2015. Water-fluxed melting of the continental crust: A review. Lithos S 212–215, 158–188.
Wiedenbeck, M., Allé, P., Corfu, F., Griffin, W.L., Meier, M., Oberli, F., Quadt, A.V., Roddick, J. C., Spiegel, W., 1995. Three natural zircon standards for U-Th-Pb, Lu-Hf, trace element and REE analyses. Geostand. Geoanal. Res. 19, 1–23.
Wu, F.Y., Yang, Y.H., Xie, L.W., Yang, J.H., Xu, P., 2006. Hf isotopic compositions of the standard zircons and baddeleyites used in U–Pb geochronology. Chem. Geol. 234, 105–126.
Wu, H., Li, C., Xu, M., Li, X., 2015. Early cretaceous adakitic magmatism in the Dachagou area, northern Lhasa terrane, Tibet: implications for slab roll-back and subsequent slab break-off of the lithosphere of the Bangong–Nujiang Ocean. J. Asian Earth Sci. 97, 51–66.
Wu, F., Liu, X., Ji, W., Wang, J., Yang, L., 2017. Highly fractionated granites: Recognition and research. Sci. China Earth Sci. 60, 1201–1219.
Xu, R.-H., Schärer, U., Allègre, C.J., 1985. Magmatism and metamorphism in the Lhasa Block (Tibet): a geochronological study. J. Geol. 93, 41–57.
Yang, Z.-Y., Wang, Q., Zhang, C., Dan, W., Zhang, X.-Z., Qi, Y., Xia, X.-P., Zhao, Z.-H., 2018. Rare earth element tetrad effect and negative Ce anomalies of the granite porphyries in southern Qiangtang Terrane, central Tibet: New insights into the genesis of highly evolved granites. Lithos 312-313-258-273.
Zeng, L., Saleeby, J.B., Asimow, P., 2005. Nd isotope disequilibrium during crustal anatexis: a record from the Goat Ranch migmatite complex, southern Sierra Nevada batholith, California. Geology 33, 53–56.
Zeng, L.J., Niu, H.C., Bao, Z.W., Yang, W.B., 2017. Chemical lattice expansion of natural zircon during the magmatic-hydrothermal evolution of A-type granite. Am. Mineral. 102, 655–665.
Zhang, H.F., Harris, N., Parrish, R., Kelley, S., Zhang, L., Rogers, N., Argles, T., King, J., 2004. Causes and consequences of protracted melting of the mid-crust exposed in the North Himalayan antiform. Earth Planet. Sci. Lett. 228, 195–212.
Zhang, K.-J., Zhang, Y.-X., Tang, X.-C., Xia, B., 2012. Late Mesozoic tectonic evolution and growth of the Tibetan plateau prior to the Indo-Asian collision. Earth Sci. Rev. 114, 236–249.
Zhang, X.Z., Wang, Q., Dong, Y.S., Zhang, C., Li, Q.Y., Xia, X.P., Xu, W., 2017. High-pressure granulite facies overprinting during the exhumation of eclogites in the Bangong-Nujiang Suture Zone, Central Tibet: link to Flat-Slab subduction. Tectonics 36.
Zhu, D.-C., Li, S.-M., Cawood, P.A., Wang, Q., Zhao, Z.-D., Liu, S.-A., Wang, L.-Q., 2016. Assembly of the Lhasa and Qiangtang terranes in Central Tibet by divergent double subduction. Lithos 245, 7–17.